Modeling the Effects of Topography Heterogeneity and Discharge Variations on Riverbed Hydrodynamics in a 30-kilometer-long Reach over a Nine-year Period using OpenFOAM

Yunxiang Chen[1], Jie Bao[1], Yilin Fang[1], Timothy Scheibe[1], Marshall Richmond[1], William Perkins[1], Huiying Ren[1], , Xuehang Song[1], Zhuoran Duan[1], Zhangshuan Hou[1], Xiaoliang He[1]

[1]Pacific Northwest National Laboratory, Richland, WA, USA

Key Points:

- Three-dimensional streamflow modeling is feasible and conducted over a 30-kilometer-long reach spanning 9 years
- A distributed roughness wall model enables short-, medium-, and long-term prediction of stream stage
- Riverbed dynamic pressure is independent of flow rate and large topographic features and follows a normal distribution

Corresponding author: Yunxiang Chen, yunxiang.chen@pnnl.gov

Abstract

Quantifying the multiscale feedback between hydrodynamics and biogeochemistry is key to reliable predictive models of river corridor systems. However, accurate and efficient hydrodynamics models over large spatiotemporal scales have not yet been established due to limited surveys of riverbed roughness and high computational costs. This work presents a semi-automated workflow that combines topographic and water stage surveys, three-dimensional computational fluid dynamics modeling, distributed wall resistance modeling, and high-performance computing to simulate the flow in a 30-kilometer river reach at the Columbia River spanning the years 2011-2019. The results show that such a workflow enables a high accuracy in modeling water surface elevation at all seven survey locations during both calibration (1 month) and validation (65 months) periods. It also enables a high computational efficiency to model the streamflow during a 58-month solution time within less than a 6-day wall clock time with the mesh number, time step, and total central processing unit hours of about 1.2 million, 3 seconds, and 1.1 million hours, respectively. Using the well-validated results, the dependencies of riverbed hydrodynamics (e.g., dynamic pressure, shear stress, and hydrostatic pressure) on flow rate non-stationarity and bathymetry spatial heterogeneity are further analyzed. These analyses show that riverbed dynamic pressure is randomly distributed over all spatiotemporal scales with its cross-sectional average values approximately quantified by a normal distribution with a mean and standard deviation of -0.353 m and 0.0352 m; bed shear stress is affected by flow rate and large- and small-scale topographic features with cross-sectional maximum values following a smooth but asymmetric distribution with 90% of its value falling in the range of 5 Pa to 35 Pa; and hydrostatic pressure is influenced by flow rate and large-scale topographic features with cross-sectional maximum values quantified by a discontinuous and skewed distribution determined by streamwise geometric variations.

Plain Language Summary

Maintaining the riverine ecosystem health depends on accurate prediction of the fluid motions and interconnected biogeochemical processes within river corridor systems. However, accurate predictive models have not yet been established due to the knowledge gaps of the multiscale feedback between flow and biogeochemistry and the high computational costs to model the diverse spatiotemporal scales. As the flowing water is the pri-

mary feature of riverine ecosystems, establishing a model that can accurately and efficiently predict the fluid dynamics within large-scale rivers over long time periods is a first step towards accurate predictive models for river corridor systems. By combining field surveys, computational fluid dynamics (CFD) modeling, and efficient numerical techniques, this work presents a semi-automated workflow that enables accurate and efficient three-dimensional CFD modeling of the streamflow in a 30-kilometer-long river reach in the Columbia River spanning a 9-year period. The modeling results show that the spatial distributions of riverbed hydrodynamics are mainly controlled by large and small topographic features, approximately independent of time; however, their values are modulated by the temporal variations in discharge. With such a model and new insights, this work provides a general framework to study the interactions between streamwater and groundwater and the multiscale feedback between fluid motions and biogeochemical processes.

1 Introduction

River corridor systems are dynamic combinations of water; sediments; chemicals; and aquatic microbes, plants, and animals (Wampler, 2012). The distinct physical, chemical, and biological behaviors of these components create diverse hydro-biogeochemical (HBGC) functions for river ecosystems over abroad temporal and spatial scales (Boano et al., 2014; Harvey, 2016; Ward & Packman, 2019). Depending on the different physical properties, a river cross section is usually divided into three zones (i.e., streamwater, hyporheic zone, and groundwater) from the water surface down to porous riverbeds to subsurface clay and rock (Boano et al., 2014; Harvey, 2016). Due to active exchanges of water, sediments, nutrients, carbon, and oxygen at the riverbed, accurate prediction of the hydrodynamics, sediment transport, chemical reactions, and microbial community dynamics at the riverbed over multiple temporal (seconds to years (Boano et al., 2014)) and spatial (microns to tens of kilometers (Ongley, 1996; Goyal, 2014; Ward & Packman, 2019)) scales are key to accurate predictive models for river corridor systems.

Among these processes, riverbed hydrodynamics and turbulence, which are determined by river slope, cross-sectional shape, riverbed microtopography, and flow rate, are key controls of the geomorphological and biochemical processes. In geomorphology, suspended load, bedload, and sediment mobilization are directly controlled by turbulence (Ongley, 1996; Venditti et al., 2010; Salim et al., 2017; Lamb et al., 2017; Yang & Nepf, 2018). In biology, population and distribution of microbes are affected by nutrient and energy absorption that depend on the availability of oxygen strongly affected by the fluctuation of water stage (Battin & Sengschmitt, 1999; Stegen et al., 2016; Trinci et al., 2017; Wilkes et al., 2019). Finally, in chemistry, stream turbulence and shear stress control the upper limit of the mass transfer rate during denitrification (Grant, Azizian, et al., 2018). These mechanisms highlight the primary importance to establish numerical models for riverbed turbulence and hydrodynamics over large spatiotemporal scales, which lays a foundation for comprehensive HBGC models for river systems.

Despite the importance of direct modeling of riverbed turbulence and hydrodynamics, implementing numerical models capable of resolving turbulence and bed hydrodynamics over natural riverbeds are still challenging, especially for large-scale rivers over long time periods. Firstly, these models are usually required to resolve both the three-dimensional (3D) coherent structures generated by streambed roughness (Hardy et al.,

2010; Grant, Gomez-Velez, & Ghisalberti, 2018; Groom & Friedrich, 2019) and the dynamically changing water surface controlled by large discharge fluctuations during a long time period (Niehus et al., 2014). Secondly, the tremendous scale separations in both spatial and temporal domains impose numerical obstacles for these models to capture the effects of spatial heterogeneity and discharge unsteadiness on riverbed hydrodynamics and its interactions with biogeochemistry (Ward & Packman, 2019). For example, to model the effects of both small-scale coarse-grain-sediments (2 mm $\sim$ 0.256 m (Ongley, 1996; Berenbrock & Tranmer, 2008)) and large-scale river valleys (0 $\sim$ 20 m) and widths (hundreds of meters), computational meshes need to vary from millimeters to meters to capture necessary scales, which poses challenges for mesh generation, numerical stability, and computational efficiency. In addition, due to the limited resolution of riverbed topography, the effect on riverbed flow dynamics has to be calibrated using observations, which may be subject to uncertainties from the calibration approach and field surveys, especially over a long time period (Schilling et al., 2019). Finally, resolving the diverse spatiotemporal scales of turbulent flows requires high computational costs. Due to these challenges, only a few 3D computational fluid dynamics (CFD) models have been reported to simulate the turbulent flow in large-scale (up to 7 km) natural rivers, though limited to steady or short-term (a few hours) time periods (Khosronejad et al., 2016; Munoz & Constantinescu, 2018). Applying these models to simulate streamwater, therefore, requires new strategies for model calibration and a significant boost of computational efficiency.

To address the above scientific and modeling challenges, this work proposes a semi-automated workflow that enables accurate and efficient 3D CFD modeling of streamflow over a 30-kilometer-long reach in the Columbia River spanning 9 years. The model results are then used to identify the dependencies of riverbed hydrodynamics (e.g., hydrostatic pressure, hydrodynamic pressure, and bed shear stress) on riverbed geometry and flow rate. The potential of extending this model to study interactions between hydrodynamics and biogeochemistry and to reduce boundary condition uncertainty in subsurface models are then discussed for future applications.

2 Methods

2.1 River bathymetry and water stage survey

The 30-kilometer-long reach is near the Hanford Site (black box) (www.hanford.gov) as shown in Figure 1a. The riverbed bathymetry was measured using a Light Detection and Ranging (LiDAR) technique with less than 1 m resolution in vertical and 20 m resolution in horizontal directions, which is used as a geometric boundary in the CFD model. Water stage was measured in three periods at seven locations (red and yellow dots in Figure 1b) every 10 minutes: at 100B, 100N, 100D, Locke Island (LI), 100H, and 100F during 2011 (observation 1); at 100B during 2013 and 2014 (observation 2); and at 100HD during 2018 and 2019 (observation 3). Water stages measured from 20 January to 16 February 2011 are used for model calibration. Measurements during the other dates in 2011 are used for short-term validation, while measurements during 2013 and 2014 are used for medium-term validation, and those during 2018 and 2019 are used for long-term validation. Here short, medium, and long term are used to represent less than 1 year, 3 to 5 years, and 8 to 9 years away from the calibration time period. The survey location 100HD is used to test the long-term model performance in predicting water surface elevation (WSE) outside the calibration locations. Horizontal coordinates and bed elevation of these locations are listed in Table S1. For convenience, the horizontal coordinates at the lower left corner of the computational domain (blue box) is converted from (564,303.5598 m, 143,735.6771 m) in the geographic information system map to (0,0) in the model domain. All vertical coordinates are referenced to North American Vertical Datum of 1988.

2.2 Free surface tracking and turbulence model

Quantifying water surface elevation, bed pressure, and shear stress requires accurate solution to the water-air interface and turbulent flow. In this work, we track the water-air interface using the volume of fluid method (Hirt & Nichols, 1981; Deshpande et al., 2012) and simulate the turbulent flow using a time-averaged Navier-Stokes equation together with $k-\omega$ shear stress transport (SST) model for turbulence closure (Menter et al., 2003; Wilcox, 2006).

The volume of fluid method marks a cell filled with liquid as $\alpha = 1$, filled with air with $\alpha = 0$, and partially filled liquid as $0 < \alpha < 1$. Denoting densities and viscosities of the liquid and gas by ρ_l, ρ_g, μ_l, and μ_g, then the density and viscosity of each cell is

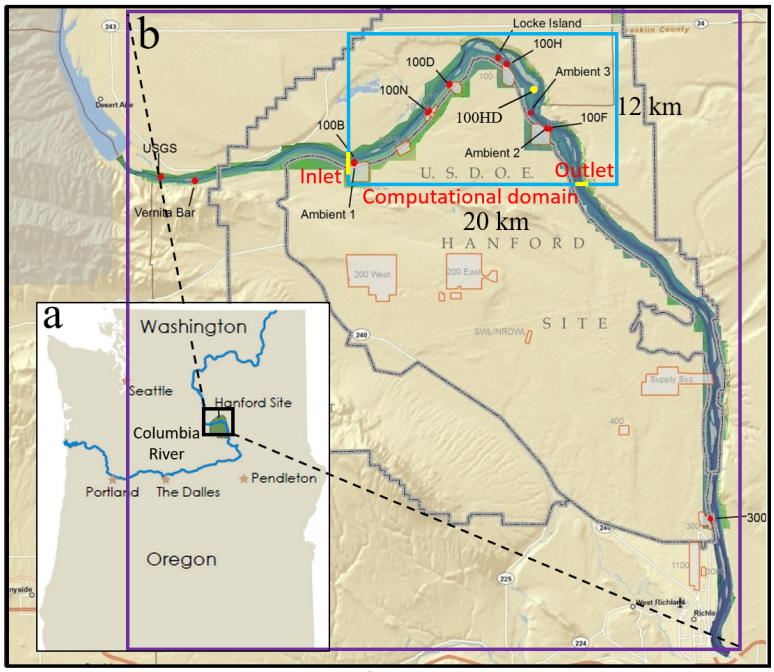

Figure 1. The location of study site within Washington State and the Columbia River (a) and the computational domain with the river bathymetry and observed water stage at seven locations (b). Yellow lines represent the inlet and outlet locations of the computational domain. Red and yellow dots denote water stage survey locations.

$\rho = \alpha\rho_l + (1-\alpha)\rho_g$ and $\mu = \alpha\mu_l + (1-\alpha)\mu_g$. Following these definitions, the time averaged Navier-Stokes equation can be written as Equation 1 and Equation 2. The governing equation for volume fraction α can be written as Equation 3 with the assumption $\frac{\rho_g}{\rho_l - \rho_g}\nabla \cdot \vec{u} \approx 0$ when $u_0 \ll c$ with u_0 and c denoting a characteristic flow velocity and the speed of sound (Kundu et al., 2012).

$$\nabla \cdot \vec{u} = 0 \tag{1}$$

$$\frac{\partial \rho\vec{u}}{\partial t} + \nabla\cdot(\rho\vec{u}\vec{u}) = \sigma\kappa_\alpha\nabla\alpha - \vec{g}\cdot\vec{x}\nabla\rho - \nabla p_d + \nabla\cdot\Big[(\mu+\mu_t)\nabla\vec{u}\Big] - \nabla\cdot\Big[(\mu+\mu_t)(\nabla\vec{u}^T - \frac{2}{3}\nabla\cdot\vec{u}\mathbf{I})\Big] \tag{2}$$

$$\frac{\partial \alpha}{\partial t} + \nabla\cdot(\vec{u}\alpha) + \nabla\cdot\Big[\alpha(1-\alpha)\vec{u}_r\Big] = 0 \tag{3}$$

where t is time, $\nabla = \frac{\partial}{\partial x}\vec{e}_x + \frac{\partial}{\partial y}\vec{e}_y + \frac{\partial}{\partial z}\vec{e}_z$ represents a spatial operator with $\vec{e}_x$, $\vec{e}_y$, and $\vec{e}_z$ denoting unit vectors along x, y, and z directions. Also denoted are time average flow velocity ($\vec{u}$), surface tension coefficient (σ), interface curvature (κ_α), gravity acceleration ($\vec{g}$), spatial coordinate ($\vec{x}$), dynamic pressure (p_d), and dynamic turbulent viscosity (μ_t). Specifically, the interface curvature is calculated by $\kappa_\alpha = -\nabla\cdot(\frac{\nabla\alpha}{|\nabla\alpha|})$, the dynamic pressure p_d is defined as $p_d = p - \rho\vec{g}\cdot\vec{x}$ with p denoting the total pressure, $\vec{u}_r$ is

an artificial velocity used to reduce numerical diffusion and computational costs whose definition can be found in Deshpande et al. (2012).

The dynamic turbulent viscosity is determined through the $k-\omega$ shear stress transport model where turbulence kinetic energy (k), specific dissipation rate (ω), and dynamic turbulent viscosity (μ_t), are quantified by Equation 4 to Equation 6 (Menter et al., 2003; Wilcox, 2006; CFDDirect, 2017).

$$\frac{\partial \alpha\rho k}{\partial t} + \nabla \cdot (\alpha\rho\vec{u}k) - \nabla \cdot \Big[\alpha(\mu + \sigma_k\mu_t)\nabla k\Big] = \alpha\rho P_k - \frac{2}{3}\alpha\rho k\nabla\cdot\vec{u} - \alpha\rho\beta^*\omega k \tag{4}$$

$$\frac{\partial \alpha\rho\omega}{\partial t} + \nabla \cdot (\alpha\rho\vec{u}\omega) - \nabla \cdot \Big[\alpha(\mu + \sigma_\omega\mu_t)\nabla\omega\Big] = \alpha\rho\gamma P_\omega - \frac{2}{3}\alpha\rho\gamma\omega\nabla\cdot\vec{u} - \alpha\rho\beta\omega^2 - \alpha\rho(F_1 - 1)\frac{CD_{k\omega}}{\omega} \tag{5}$$

$$\mu_t = \frac{a_1\rho k}{\max(a_1\omega, b_1F_2\sqrt{2S^2})} \tag{6}$$

where $\sigma_k = \alpha_{k1}F_1 + \alpha_{k2}(1 - F_1)$, $P_k = \min(G, c_1\beta^*k\omega)$, $\sigma_\omega = \alpha_{\omega1}F_1 + \alpha_{\omega2}(1 - F_1)$, $\gamma = \gamma_1F_1 + \gamma_2(1 - F_1)$, $P_\omega = \min\Big[S^2, \frac{c_1\beta^*}{a_1}\omega\max(a_1\omega, b_1F_2\sqrt{2S^2})\Big]$, $CD_{k\omega} = \max(10^{-10}, \frac{2\alpha_{\omega2}\nabla k\cdot\nabla\omega}{\omega})$. F_1 and F_2 are blending functions and defined as $F_1 = \tanh(arg_1^4)$ and $F_2 = \tanh(arg_2^2)$ with $arg_1 = \min\{\min[\max(\frac{1\sqrt{k}}{\beta^*\omega y_w}, \frac{500\mu}{\rho y_w^2\omega}), \frac{4\alpha_{\omega2}k}{y_w^2CD_{k\omega}^2}], 10\}$ and $arg_2 = \min[\max(\frac{2\sqrt{k}}{\beta^*\omega y_w}, \frac{500\mu}{\rho y_w^2\omega}), 100]$. Symbols β^*, $\alpha_{\omega1}$, $\alpha_{\omega2}$, α_{k1}, α_{k2}, β_1, β_2, γ_1, γ_2, and a_1, b_1, and c_1 denote constants and their values are listed in Table S2.

2.3 Mesh generation and quality control

Good mesh quality is a crucial factor controlling computational stability and efficiency, especially for free surface tracking in large-scale river modeling over the long time (Deshpande et al., 2012). In this work, the mesh is generated using a two-step generation strategy, which first generates a structured background mesh and then removes all cells totally outside a given geometry (a river bathymetry in our case). Different from the traditional body-fitted mesh, the mesh generated using such a strategy does not exactly conform to the input geometry but approximates the bathymetry using a zig-zag grid.

This treatment is both physically reasonable and technically necessary. Physically, the LiDAR-measured bathymetry cannot capture most geometric features that are smaller than 1 m, which means computational cells with size less than 1 m are not necessary. In addition, the effect of geometric features on flow dynamics, either from missing features less than 1 m or the differences attributed to mesh generation, has to be calibrated

using observed water stage through a distributed rough wall model (see details in Section 2.4). A well-calibrated model automatically accounts for the effect of bathymetry differences between the CFD mesh and actual riverbed. Technically, a good mesh quality using body-fitted meshes requires low aspect ratio in cells. However, low aspect ratio requires a similar order of mesh resolution in both the horizontal and vertical directions, which is computationally expensive for large rivers whose water depth is much smaller than its horizontal scales, about $1/20000 \sim 1/1000$ for the river section in this work.

The primary goal of this work is to model the riverbed dynamic pressure, bed shear stress, and hydrostatic pressure; therefore, we design the horizontal mesh resolution as 20 m along x and y, which is identical to the horizontal resolution in the LiDAR-measured digital elevation model (DEM). The vertical mesh resolution is set as 1 m by balancing modeling accuracy and computational costs. One extra mesh resolution, 20 m$\times$ 20 m$\times$ 0.5 m, is also created to investigate the sensitivity of modeled riverbed pressure to mesh resolution (see uncertainty analyses in Text S1). Following the two-step mesh generation strategy, Figure 2 shows the horizontal and vertical mesh in the computational domain. It is observed that the aspect ratio for horizontal (x and y) grid sizes is 1 but in the vertical direction it is 1/20. Despite such a large aspect ratio, the rectangular hexahedron cells still have a good mesh quality in terms of non-orthogonality and concavity which are important for code numerical stability. Figure 2c also shows that the zigzag grid does not overlap with the riverbed, whose effect on flow is discussed for the roughness calibration.

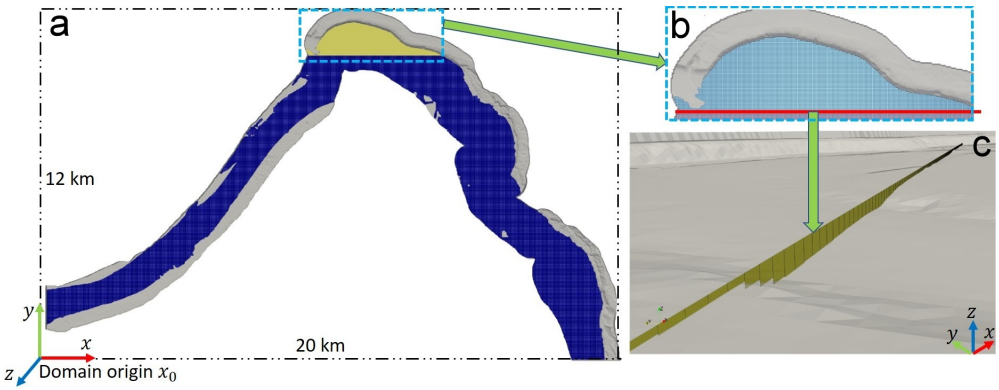

Figure 2. Horizontal and vertical computational meshes. (a) Top view showing the horizontal mesh over the whole domain. (b) Top view showing the details of horizontal mesh near LI. (c) 3D view showing details of the vertical mesh structure.

2.4 Turbulent eddy viscosity and roughness parameterization

Rough elements are ubiquitous in natural rivers and have long been recognized as the major source of uncertainty in predicting river discharge, flow speed, water surface profile, and sediment transport (USACE, 1994; Smith, 2014; Powell, 2014). In the $k-\omega$ SST turbulence model, the effect of rough elements on turbulent flow is quantified by linking riverbed turbulence eddy viscosity to bed roughness and flow conditions through Equation 7 (Versteeg & Malalasekera, 2007).

$$\nu_t = \nu[\frac{\kappa y_w^+}{\ln(E y_w^+)} - 1] \tag{7}$$

Symbols in Equation 7 denote turbulent kinematic viscosity $\nu_t = \mu_t/\rho$, kinematic viscosity $\nu = \mu/\rho$, von Karman's constant $\kappa = 0.41$, a non-dimensional wall distance $y_w^+ = \frac{y_w u_\tau}{\nu}$, and an integration constant E. The specific value of E depends on the flow regime and roughness parameter at the wall. Specifically, $E = E_0 = 9.8$ in a hydraulic smooth regime ($k_s^+ < 2.25$), $E = (\frac{k_s^+ - 2.25}{87.75} + C_s k_s^+)^{\sin[0.4258(\ln k_s^+ - 0.811)]}$ in a transition regime ($2.25 \leq k_s^+ < 90$), and $E = E_0/(1+C_s k_s^+)$ in a fully rough regime ($k_s^+ > 90$) (Schlichting, 1979; Versteeg & Malalasekera, 2007; Blocken et al., 2007; CFDDirect, 2017). Here $k_s^+ = \frac{k_s u_\tau}{\nu}$ is a non-dimensional parameter used to quantify the relative importance of a Nikuradse equivalent roughness height k_s to viscous boundary layer thickness νu_τ^{-1}.

For natural rivers, the flow is usually in the fully rough regime, which means estimation of turbulence eddy viscosity is equivalent to estimating the roughness parameters C_s and k_s and bed shear velocity u_τ. As classic theories on roughness are usually based on experiments of grain size roughness (Nikuradse, 1933), we choose $C_s = 0.5$ with the assumption that natural roughness distribution is similar to uniformly roughed channels as in Nikuradse's experiments (Blocken et al., 2007). We estimate the bed shear velocity using the turbulence boundary layer theory that links a non-dimensional velocity ($u^+ = u/u_\tau$) to the non-dimensional wall distance (y_w^+) through a wall function G, thus $u^+ = G(y_w^+)$. In the fully rough regime, the wall function follows a log-law which has the form as $u^+ = \frac{1}{\kappa}\ln y_w^+ + B - \Delta B$ with $B = 5.2$ and $\Delta B = B - 8.5 + \frac{1}{\kappa}\ln k_s^+$ (Schlichting, 1979). Substituting the velocity (u^0) and wall distance (y_w^0) at the cell center closest to the wall, the wall function is converted to a non-linear function depending on shear velocity, roughness parameter, and near-bed velocity and wall distance, thus $G(u^0, y_w^0, u_\tau, k_s) = 0$. By solving such an equation under a given roughness k_s, we can obtain the value for bed shear velocity u_τ and wall turbulent eddy viscosity ν_t.

The above procedure means solving for shear velocity requires an estimation of bed roughness height k_s. This work proposed a generic approach to estimate a distributed roughness field using an error diagram and local roughness adjustment approach. The error diagram provides a rough estimation of the roughness parameters and the local adjustment further improves calibration accuracy per the error diagram. The error diagram is based on the fact that water surface elevation increases with increasing roughness height and thus an optimal roughness height should fall in a range $0 < k_s < k_s^{max}$ in order for the model to match the observed water stage (Figure 3a and Figure S1).

In this work, the effect of rough elements larger than 1 m is directly resolved by mesh and thus an upper limit of roughness can be set as $k_s^{max} = 1$ m. With such an upper limit, we run our models at nine roughness values (0 m, 0.025 m, 0.05 m, 0.1 m, 0.2 m, 0.3 m, 0.4 m, 0.5 m, 1 m) and then calculate the mean error (ME) and mean absolute error (MAE) between modeled water stage and observed ones at six locations (Figure 1b red dots) from 20 January to 16 February 2011. With the error diagram as shown in Figure 3b and Figure S2, we calculate an optimal roughness height k_s for each observation location by making ME = 0 and MAE to be the minimum.

The optimal k_s obtained in this way is then uniformly distributed in eight regions shown in Figure 3c (see region decomposition in Section 2.6). Here k_s in R1 and R8 are identical to those in R2 and R7, respectively (Figure 3d). Due to the interactions of flow under different roughness parameters, the locally optimized roughness field does not guarantee low modeling errors at all locations (see case OF0 in Table 1). As higher deviations occur at 100B, 100N, and 100D, their roughness parameters are systematically adjusted to achieve better accuracy for all six locations (cases OF1-OF5 in Table 1). The final calibrated roughness values at the six calibration locations are listed in case OF in Table 1. These calibrated roughness parameters are then used to simulate the flow from May to December 2011, 2013-2015, and 2018-2019 to evaluate the modeling capability for short-term, medium-term, and long-term streamflow. A more comprehensive discussion of roughness estimation is included in Section 4.1.

2.5 Boundary conditions

Temporal variations in discharge at the inlet control the dynamic changes in streamflow and riverbed conditions. Figure 4 shows the temporal variations of discharge at the

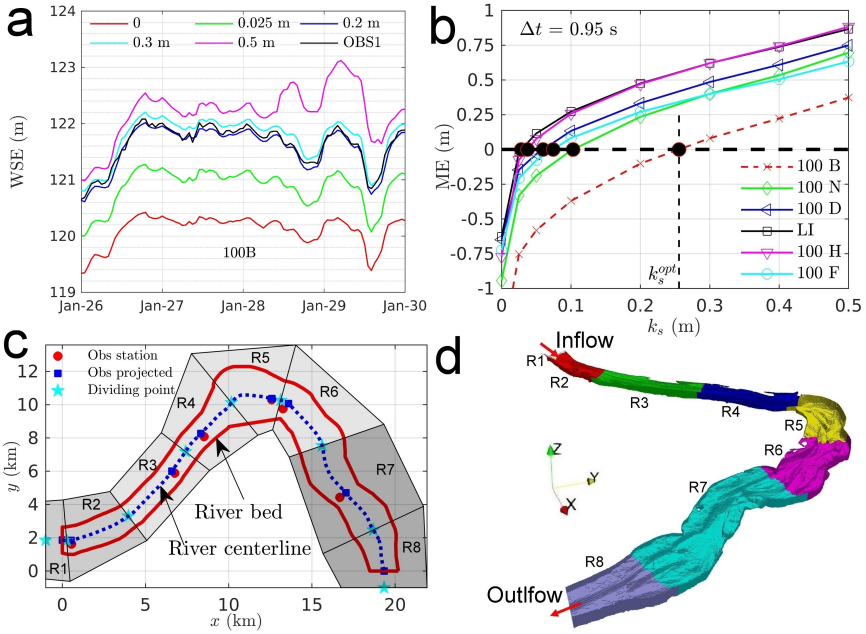

Figure 3. The effect of roughness height on WSE at a single location (a), ME between modeled and observed WSE at six locations (b), the procedure of generating eight roughness regions (c), and the 3D view of each region represented in mesh (d).

inlet during years 2011 to 2019. A two-step approach is adopted to consider the discharge effects. We first run a one-dimensional (1D) modular aquatic simulation system (MASS1) model (Richmond & Perkins, 2009) in a much larger domain using observed discharge data and then output the cross-sectional averaged velocity (u^1) and water stage (z^1) to generate a distributed velocity and volume-fraction field for the inlet in our model. Specifically, the inflow velocity and volume-fraction are calculated by $\vec{u} = (u_x, 0, 0)$ with $u_x = u_{in}^1 \frac{\text{erf}[(z_{in}^1 - z)/0.5]+1}{2}$ and $\alpha = \frac{\text{erf}[(z_{in}^1 - z)/0.5]+1}{2}$. Here u_{in}^1 and z_{in}^1 denote the velocity and water surface elevation from MASS1 at the inlet and erf is an error function. The turbulence kinetic energy and specific dissipation rate at the inlet are set as a fixed value of 0.1 m^2/s^2 and 0.003 s^{-1}, respectively. A zero-gradient boundary condition is set for dynamic pressure and turbulence eddy viscosity at the inlet. It is worth mentioning that the given values of turbulent kinetic energy and specific dissipation rate have little effect on the results. At the outlet, we apply a uniform velocity with its value output from MASS1, i.e., $\vec{u} = (0, u_y, 0)$ with $u_y = u_{out}^1$. Other boundary conditions at the outlet are zero-gradient. At the top boundary, pressure is set as 0 and the other variables are set as zero-gradient. At the riverbed, the turbulence eddy viscosity is determined through

a rough wall model as discussed in Section 2.4. A no-slip boundary condition is set for velocity and zero-gradient boundary conditions are set for dynamic pressure, volume-fraction, and turbulence kinetic energy. The specific dissipation rate is calculated through $\omega_w = (\omega_{Vis}^2 + \omega_{Log}^2)^{1/2}$ with $\omega_{Vis} = \frac{6.0\nu}{\beta_1 y_w^2}$ and $\omega_{Log} = \frac{k^{1/2}}{C_\mu^{1/4}\kappa y_w}$ (see values of β_1 and C_μ in Table S2).

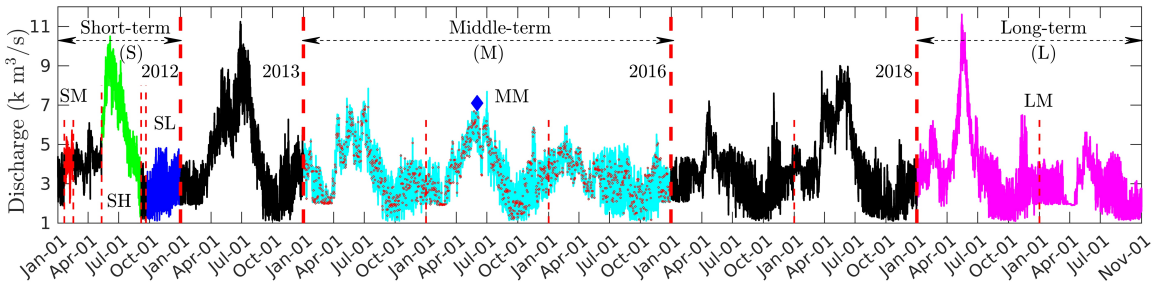

Figure 4. The time series of inlet flow rate during the years 2011-2019. S, M, and L denote short, medium, and long term. SM, SH, and SL denote the medium, high, and low flow in the short-term period; MM and LM denote mixed flow in the medium-term and long-term periods.

2.6 Spatiotemporal decomposition

Spatial and temporal decomposition techniques are used in this work to improve both modeling accuracy and computational efficiency. Firstly, surface decomposition is used to decompose the riverbed bathymetry into N pieces in order to generate a distributed roughness field (see details of surface decomposition in Text S2). We evaluated the effects of N on modeling accuracy and found that the best calibration accuracy can be achieved when the number of pieces equals the number of observation locations. For example, decomposing the riverbed into 1, 2, and 50 pieces (see roughness values and surface decomposition in Figure S3) and interpolating calibrated roughness to each piece cannot yield a modeling accuracy as that of using 6 pieces (see cases OF0, OFK1, OFK2, and OFK50 in Table 1). Further discussion of the number of pieces in surface decomposition is included in Section 4.1. Second, the computational domain is decomposed into 512 subdomains and runs on 512 processors, which increases the computational efficiency by multiple times (see discussion in Section 4.3). Thirdly, the overall computational efficiency is further improved by decomposing the total simulation time into multiple months and running each month simultaneously. In this work, we divide the medium-term (2013-2015)

and long-term (2018-2019) simulations into 36 and 22 months and add 4 extra days for each month to spin up the flow and reduce the potential time-history effect. It is important to note that the modeled water stage reaches a fully developed stage after two to three flow-through times (about $T = L/U_0 = 30000\ /0.8$ s $= 0.43$ days), which is the basis for temporal decomposition. Further discussion of the effect of temporal decomposition on computational efficiency is included in Section 4.3.

2.7 Numerical schemes and solutions

The governing equations for flow ($\vec{u}$, p_d), volume fraction (α), and turbulence (k, ω) were solved with an open-source CFD platform, OpenFOAM (Version 5.x), using a finite volume method (CFDDirect, 2017). The unsteady terms are discretized with a first-order Euler scheme, the advection term of flow is discretized with a second-order Gauss linear upwind scheme, and the advection terms of turbulent kinetic energy and specific dissipation rate are discretized with a second-order Gauss linear scheme. The advection term and the compression term of volume fraction are discretized with Gauss vanLeer and Gauss linear schemes, respectively. All diffusion terms are discretized with a corrected central differencing scheme and all gradient terms are discretized with a second-order central differencing method. With these discretization schemes and initial conditions, OpenFOAM first updates the volume fraction at the interface using a Multidimensional Universal Limiter with Explicit Solution (MULES) algorithm (Zalesak, 1979; Kuzmin et al., 2003; Liu et al., 2016), and then solves the velocity-pressure coupling using a Pressure Implicit with Splitting of Operators (PISO) algorithm (Issa, 1985), followed by solving ω and k equations. At each iteration, the discretized linear equation group for pressure is solved using a Diagonal-based Incomplete Cholesky Preconditioned conjugate gradient (DIC-PCG) method with a relative convergence tolerance of 10^{-10}, and the discretized linear equation groups for velocity, volume fraction, turbulent kinetic energy, and specific dissipation rate are solved with a symmetric Gauss-Seidel smooth solver at a relative tolerance 10^{-10}. The initial time step is set as 10^{-10} s but allowed to adjust during runtime to not exceed 3 s. The maximum and average Courant number for all cases are less than 1.1 and 0.019, respectively. With the solution of volume fraction, the water surface elevation is calculated by setting $\alpha = 0.5$ (Hirt & Nichols, 1981). It is necessary to note that the modeled water surface elevation changes little at time steps 0.1

s, 0.5 s, 0.95 s, 2 s, and 3 s (see Figure S4); therefore, the maximum time step is chosen as 3 s to reduce computational costs.

3 Results

3.1 Short-term roughness calibration

The error diagram approach gives a rough estimation of the hydraulic roughness at each location. The modeling accuracy using these roughness parameters are -16.5 cm $\sim$ 6.4 cm and 7.6 cm $\sim$ 19.6 cm at six locations (Case OF0 in Table 1) in terms of ME and MAE, respectively. By systematically adjusting the roughness parameters at 100B, 100N, and 100D, the overall modeling accuracy is improved. Figure 5 compares the water surface elevation using the locally adjusted roughness field (Case OF in Table 1) and those from observation 1. The comparison of the hourly recorded water stage data shows the modeled WSE accurately predicts the magnitude and frequency in the WSE. The 1:1 plot shows there is no systematic bias in the model, which can be further demonstrated by an R-squared (R^2) and linear-regression slope very close to 1 (Table 2 SM cases). Here $R^2 = 1 - \frac{\sum(WSE_m - WSE_o)^2}{\sum(WSE_m - \overline{WSE}_o)^2}$, $\overline{WSE}_o = \frac{\sum WSE_o}{N_t}$ with WSE_m, WSE_o, and N_t denoting modeled WSE, observed WSE, and the number of time series, respectively. Quantitatively, the ME at the six locations falls in the range -7.5 cm $\sim$ 6.4 cm, which is equivalent to -2.7% $\sim$ 2.1% relative to the average water depth at each location. The MAE at all locations is 7.5 cm $\sim$ 12.7 cm, which is equivalent to 2.1% $\sim$ 5.3% relative to water depth. The root mean square, defined as RMS $= \sqrt{\frac{\sum(WSE_m - WSE_o)^2}{N_t}}$, for all locations is 9.2 cm $\sim$ 16.4 cm, which is equivalent to 2.8% $\sim$ 6.3% relative to the average water depth at each location.

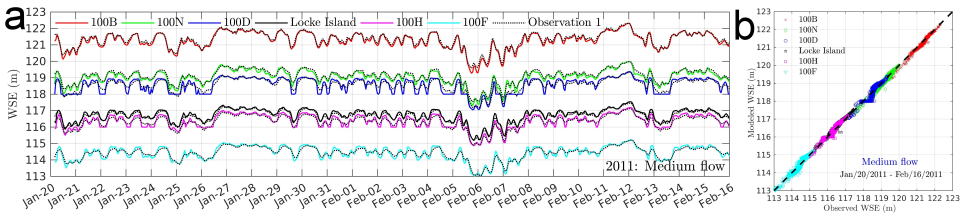

Figure 5. The comparison of water surface elevation between the model and observations using the calibrated roughness field (case OF in Table 1) during a medium flow in 2011. (a) An hourly recorded WSE and (b) a 1:1 plot.

Table 1. Roughness adjustment approach and associated ME and (MAE).

Case	Calibrated k_s (cm)						ME during 1/20-2/16, 2011 (cm)							MAE during 1/20-2/16, 2011 (cm)						
name	100B	100N	100D	LI	100H	100F	100B	100N	100D	LI	100H	100F	Range	100B	100N	100D	LI	100H	100F	Range
OF0	25.56	10.3	5.98	2.83	3.74	7.42	-16.5	-19.5	-6.8	6.4	4.8	0.3	-16.5∼6.4	16.5	19.6	12.7	7.6	8.9	9.3	7.6∼19.6
OF1	30	10.3	5.98	2.83	3.74	7.42	-11.1	-19.5	-7.4	6.4	3.3	0.3	-19.5∼6.4	11.2	19.6	13.4	7.6	10.1	9.3	7.6∼19.6
OF2	40	10.3	5.98	2.83	3.74	7.42	-0.6	-19.5	-7.4	6.4	3.3	0.3	-19.5∼6.4	5.8	19.6	13.4	7.6	10.1	9.3	7.6∼19.6
OF3	40	18.6	5.98	2.83	3.74	7.42	1.6	-16.8	-7.2	6.4	3.4	0.4	-16.8∼6.4	6.5	17.0	13.3	7.6	10.1	9.3	7.6∼17.0
OF4	30	18.6	5.98	2.83	3.74	7.42	-8.7	-16.9	-7.4	6.4	3.3	0.3	-16.9∼6.4	9.1	17.0	13.3	7.5	10.1	9.2	7.5∼17.0
OF5	30	18.6	9.0	2.83	3.74	7.42	-7.5	-11.7	-3.6	6.4	3.3	0.3	-11.7∼6.4	8.2	12.2	12.6	7.5	10.0	9.2	7.5∼12.6
OF	30	18.6	12.0	2.83	3.74	7.42	-6.6	-7.5	-0.6	6.4	3.3	0.3	-7.5∼6.4	7.7	8.9	12.7	7.5	10.0	9.2	7.5∼12.7
OFK1	12.2	12.2	12.2	12.2	12.2	12.2	-29.1	6.6	17.7	32.1	31	13.1	-29.1∼32.1	29.1	7.5	19.5	32.6	31.5	14.6	7.5∼29.1
OFK2	25.56	6.25	6.25	6.25	6.25	6.25	-16.7	-15.0	1.3	14.8	12.2	13.1	-16.7∼14.8	16.7	15.2	12.2	15.1	13.4	9.2	9.2∼15.2
OFK2R	25.56	6.25	6.25	6.25	6.25	6.25	-14.1	-14.9	1	14.8	12.3	-3.7	-14.9∼14.8	14.1	15.1	12.3	15.1	13.4	9.1	9.1∼15.1
OFK50	see Figure S3						-19.4	-18.8	-6.1	8.5	8	1.4	-19.4∼8.5	19.4	18.8	12.5	9.3	10.5	9.7	9.3∼19.4
MS	30.5	18.6	15.6	3.9	3.9	7.42	-4.7	-1.2	4.9	7.7	3.9	0.3	-4.7∼7.7	6.7	6.4	13.9	8.6	10.3	9.2	6.4∼13.9
MS2	30.5	18.6	12.0	3.9	3.9	7.42	-5.6	-5.6	1.9	7.7	3.8	0.2	-5.6∼7.7	7.1	7.8	12.9	8.5	10.2	9.2	7.1∼12.9
MS3	30.5	18.6	9.0	3.9	3.9	7.42	-6.6	-9.8	-1.0	7.7	3.8	0.2	-9.8∼7.7	7.6	10.6	12.5	8.6	10.2	9.2	7.6∼12.5

3.2 Short-term model validation

Though this work calibrates the distributed roughness field using the observed WSE at a medium flow (discharge 4227 m^3/s) scenario, we show that calibrated roughness works well for predicting the WSE at high flow (6335 m^3/s) and low flow (2613 m^3/s) scenarios. Figure 6 compares the hourly recorded WSE with observations during high flow (Figure 6a) and low flow (Figure 6c). Figure 6b,d shows the 1:1 comparison between these data. The results show a good match in terms of the magnitude and frequency of the WSE at the six locations. The 1:1 plot shows there is no obvious bias in modeled WSE. In statistics, the ME during high flow is -2.5 cm $\sim$ 9.1 cm, which is equivalent to -0.6% $\sim$ 1.9% relative to mean water depth at each location. Similarly, these values at low flow is -15.6 cm $\sim$ 5.5 cm and -7.1% $\sim$ 6.6%, respectively. In terms of the MAE, it is 7.2 cm $\sim$ 13.5 cm (1.5% $\sim$ 3.1% relative to average water depth) at high flow and 13.1 cm $\sim$ 26.6 cm (5.1% $\sim$ 15.8% relative to water depth) at low flow. The RMS is 9.7 cm $\sim$ 15.9 cm (2.0% $\sim$ 3.8% relative to water depth) at high flow and 17.7 cm $\sim$ 40.3 cm (6.9% $\sim$ 22.2% relative to water depth) at low flow. The calculated R^2 for the difference between modeled and observed WSE is larger than 0.98 for six locations at high flow and is in the range 0.88 - 0.93 at low flow, except for at 100D where the value is 0.603. The slope of the linear regression has a similar trend as R^2 that it falls in the range 1.05 - 1.1 during high and low flow at most locations, however has a value of 0.859 at 100D during low flow. These results suggest that the modeled WSE agrees with observation very well at all locations during the high flow event. The model WSE is less accurate at low flow and

has obvious deviation at locations where the water depth is less than 1 m (case SL at 100H) or not available due to being too close to the wet/dry boundary (100D).

Table 2. A summary of flow scenario, discharge, water depth, roughness height, and modeling accuracy for calibration, validation, and prediction.

Survey Station	Time Period	Year	Month Day	Flow Scenario	Mean Discharge (m^3/s)	Mean depth (m)	k_s cm	WSE: OF-Observed ME cm	RME %	MAE cm	RMAE %	RMS cm	RRMS	R^2 %	β
100B	SM	2011	1/20-2/16	Medium	4227	3.57	30	-6.6	-1.8	7.7	2.1	10.1	2.8	0.963	1.072
	SH	2011	5/11-9/6	High	6335	4.88		-2.1	-0.4	7.2	1.5	9.7	2.0	0.994	1.062
	SL	2011	9/20-12/31	Low	2613	2.19		-15.6	-7.1	19.7	9.0	25.4	11.6	0.914	1.102
	MH[2]	2013	3/11-6/19	High	4449	3.65		-10.1	-2.8	11.9	3.3	15.1	4.1	0.982	1.083
	ML[2]	2013-14	9/27-1/5	Low	2517	2.10		-20.7	-9.9	22.4	10.7	26.4	12.6	0.879	1.108
	MH[2]	2014	4/15-7/24	High	5217	4.27		-9.2	-2.2	10.5	2.5	13.3	3.1	0.945	1.053
	MM[2]	2013-14	1/1-8/1	Mixed	3755	3.12		-14.4	-4.6	16.1	5.2	22.1	7.1	0.965	1.065
100N	SM	2011	1/20-2/16	Medium	4227	2.78	18.6	-7.5	-2.7	8.9	3.2	10.9	3.9	0.943	1.031
	SH	2011	5/11-/9/6	High	6335	3.96		-2.5	-0.6	8.9	2.2	11.0	2.8	0.991	1.058
	SL	2011	9/20-12/31	Low	2613	1.58		-10.3	-6.5	19.9	12.6	26.1	16.4	0.881	1.061
	MM	2013-15	1/1-12/31	Mixed	3424	2.17		NA	NA	NA	NA	NA	NA	NA	NA
100D	SM	2011	1/20-2/16	Medium	4227	NA	12	-0.6	NA	12.7	NA	16.4	NA	0.874	1.149
	SH	2011	5/11-/9/6	High	6335	NA		3.1	NA	10.6	NA	13.7	NA	0.983	1.071
	SL	2011	9/20-12/31	Low	2613	NA		-1.8	NA	26.6	NA	40.3	NA	0.603	0.859
	MM	2013-15	1/1-12/31	Mixed	3424	NA		NA	NA	NA	NA	NA	NA	NA	NA
LI	SM	2011	1/20-2/16	Medium	4227	2.99	2.83	6.4	2.1	7.5	2.5	9.2	3.1	0.948	1.023
	SH	2011	5/11-/9/6	High	6335	4.02		NA	NA	NA	NA	NA	NA	NA	NA
	SL	2011	9/20-12/31	Low	2613	1.91		NA	NA	NA	NA	NA	NA	NA	NA
	MM	2013-15	1/1-12/31	Mixed	3424	2.44		NA	NA	NA	NA	NA	NA	NA	NA
100H	SM	2011	1/20-2/16	Medium	4227	1.90	3.74	3.3	1.7	10.0	5.3	12.0	6.3	0.923	1.073
	SH	2011	5/11-/9/6	High	6335	3.00		5.7	1.9	9.2	3.1	11.3	3.8	0.989	1.053
	SL	2011	9/20-12/31	Low	2613	0.83		5.5	6.6	13.1	15.8	18.4	22.2	0.922	1.062
	MM	2013-15	1/1-12/31	Mixed	3424	1.36		NA	NA	NA	NA	NA	NA	NA	NA
100F	SM	2011	1/20-2/16	Medium	4227	3.66	7.42	0.3	0.08	9.2	2.5	11.5	3.1	0.928	1.106
	SH	2011	5/11-/9/6	High	6335	4.77		9.1	1.9	13.5	2.8	15.9	3.3	0.978	1.103
	SL	2011	9/20-12/31	Low	2613	2.59		2.6	1.0	13.3	5.1	17.7	6.9	0.926	1.071
	MM	2013-15	1/1-12/31	Mixed	3424	3.12		NA	NA	NA	NA	NA	NA	NA	NA
100HD	LL[3]	2018-19	8/16-10/31	Low	2580	1.33	NA	7.2	5.4	14.9	11.3	22.5	17.0	0.89	0.980
	LM[3]	2018-19	1/1-10/31	Mixed	3310	1.78		7.2	4.0	14.9	8.4	22.5	12.6	NA	NA

Observation stations are illustrated in Figure 1b, the first character in "Time Period" represents short-term (S), medium-term (M), and long-term (L), and the second character in "Time period" represents medium (M), high (H), low (L), or mixed (M) type flow scenarios. Superscripts 2 and 3 denote observation data used for comparison are from observation 2 and observation 3. R^2 and β is a coefficient quantifying the degree of correlation between modeled and observed WSE and the slope of the linear regression of 1:1 plots. NA is used when observed data is not available.

3.3 Medium-term model validation

The short-term validation shows the roughness calibrated using the WSE observed at a medium flow can well predict WSE at medium, high, and low flow scenarios. To further test if the calibrated roughness can be applied for medium-term surface flow simulations, Figure 7 compares the modeled WSE with the observed WSE at 100B during 2013-2014. Figure 7a shows a comparison of the hourly recorded WSE from the model with those from two different observations. Such a comparison shows that modeled WSE agrees well with the observations from 1 January 2013 to 1 August 2014. In addition, it shows that observed WSE has uncertainties. A further comparison between the two

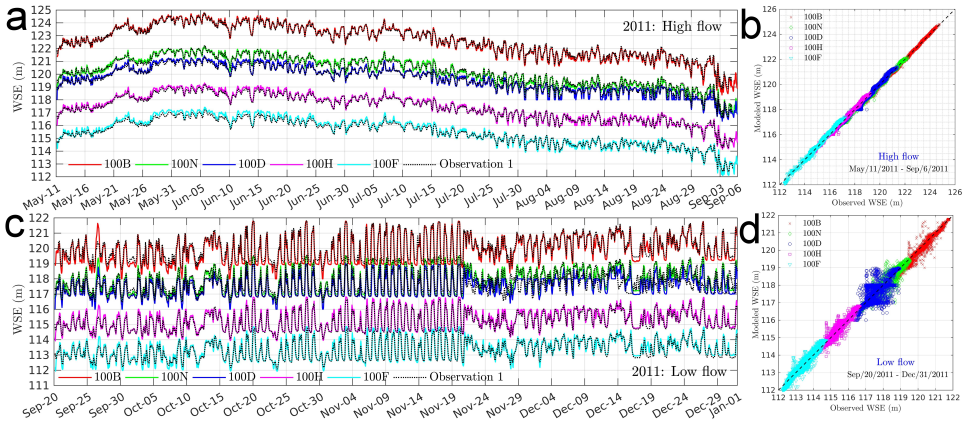

Figure 6. The comparison of water surface elevation from model and observations during high flow and low flow in 2011. (a-b) Hourly recorded time series of WSE and 1:1 plot during high flow. (c-d) Hourly recorded time series of WSE and 1:1 plot during low flow.

observations shows that WSE from observation 2 is about 3.2 cm higher than that from observation 1 and that a small shift in time results in a large error in standard deviation between the two observations (see uncertainty analyses in Text S1 and Figure S5). However, as observation 1 lacks the record during 2013-2014, observation 2 is used for validation during this time period.

As WSE observation is missing at some dates, three time periods with continual observations (see MH^2 and ML^2 in Table 2) were chosen to illustrate the modeling performance of predicting WSE as shown in Figure 7b,c,d. The comparison shows that the modeled WSE agrees very well with observations at the high flow scenarios during March-June 2013 (Figure 7b) and April-July 2014 (Figure 7d). The ME, MAE, and RMS during these periods are -10.1 cm $\sim$ -9.2 cm, 10.5 cm $\sim$ 11.9 cm, and 13.3 cm $\sim$ 15.1 cm, respectively. The corresponding relative error to average water depth is -2.8% $\sim$ -2.2%, 2.5% $\sim$ 3.3%, 3.1% $\sim$ 4.1%, respectively. At the low flow during September 2013-January 2014 (Figure 7d), the model shows a larger error especially when the WSE is low (close to 119 m). However, the relative errors to water depth are still small, -9.9%, 10.7%, and 12.6% for relative ME, MAE, and RMS (see ML^2 in Table 2), respectively. Figure 7e,f,g further shows a 1:1 comparison between modeled and observed WSE. The R^2 and the linear regression slope are 0.88 $\sim$ 0.98 and 1.06 $\sim$ 1.1, respectively. These results suggest the predicted WSE has no obvious bias and the prediction has good accuracy for a medium-term prediction.

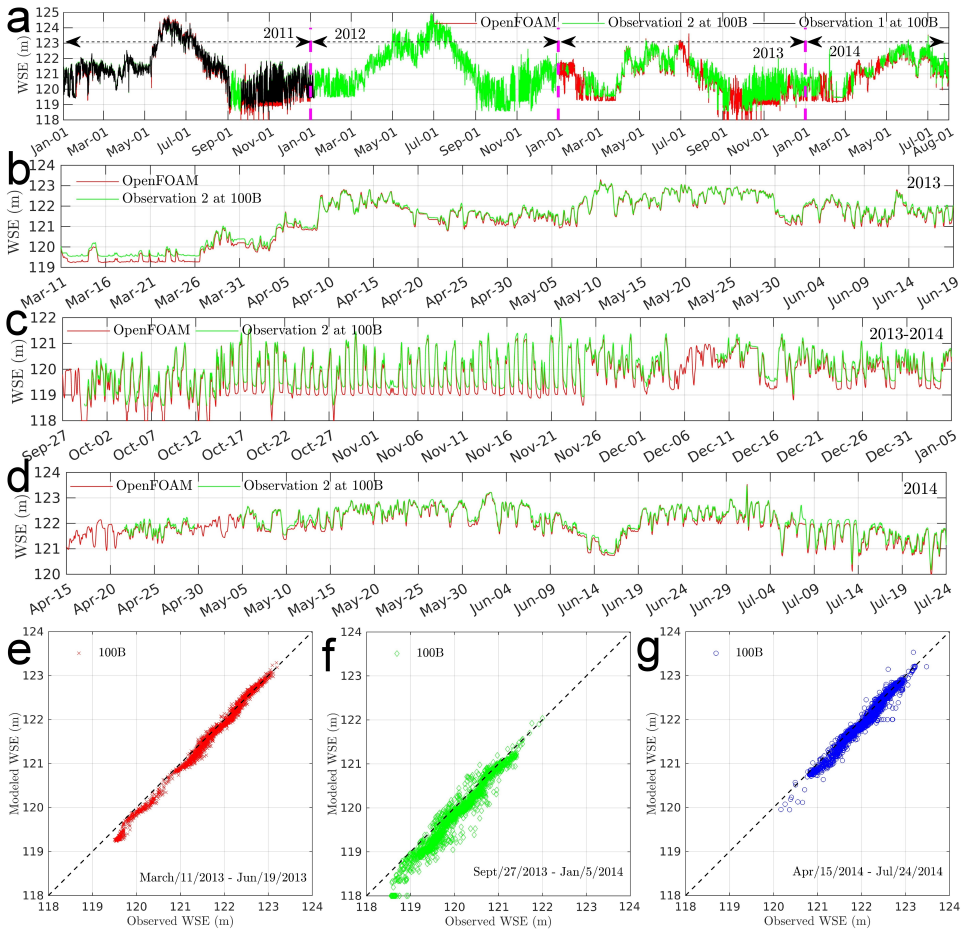

Figure 7. Medium-term model validation for water surface elevation. A comparison of hourly recorded WSE from model and observations during 2011-2014 (a), medium flow (b), low flow (c), and high flow (d). (e-g) denote the 1:1 plot during medium, low, and high flow scenarios.

3.4 Long-term model validation

The long-term prediction of WSE is important for predicting river corridor function under a long-term climate change scenario. To test the modeling performance for long-term WSE prediction, Figure 8 compares the WSE from the model and the observation at one location (yellow dot in Figure 1b), different from the locations used for calibration. Figure 8a shows that the model well captures the trend of the fluctuation in WSE at 100HD during August 2018-November 2019. The ME and MAE are 7.2 cm and 14.9 cm, respectively. This is equivalent to 5.4% and 11.3% relative to the mean water depth. The RMS is 22.5 cm and about 17.0% relative the average water depth at 100HD during August 2018-November 2019. Figure 8b further shows the 1:1 plot between the

modeled and observed WSE at 100HD. The R^2 and linear regression slope are 0.89 and 0.980, respectively. These statistics show there is no obvious bias in our model as the slope is very close to 1. As the flow during August 2018-November 2019 is always low (2580 m^3/s), the R^2 during this time period is similar to those calculated at low flow scenario (see SL at 100B-100F in Table 2) in 2011-2015. Similarly, a lower R^2 is also related to a small time shift in the observation as shown in Figure S5. Considering that a small time shift in the observation results in a significant error in MAE and RMS, the ME is a more reliable index for evaluating the modeling accuracy. Therefore, it is reasonable to claim that our model is able to predict WSE in 2018 and 2019 with an accuracy of 5.4% relative to mean water depth using the roughness calibrated in 2011. This suggests that in the next 9 years the WSE may be reliably predicted using the calibrated roughness at the present time.

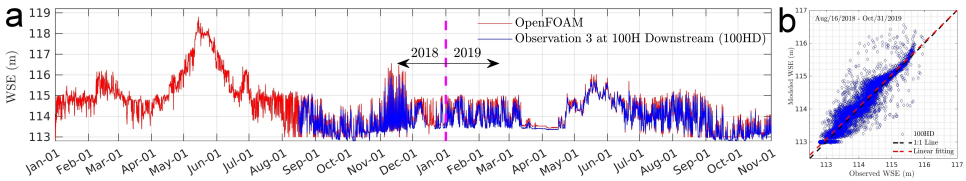

Figure 8. Long-term model validation for water surface elevation. A comparison of the hourly recorded WSE from model and observations at 100HD during 2018-2019 (a), and their 1:1 plot (b).

3.5 Controls of bed hydrodynamics

As bed hydrodynamics control the mass exchange and concentration fluxes at the riverbed, identifying their control mechanisms is helpful for quantifying hydrologic exchange flows (HEFs) and residence time distributions (RTDs), which is important for parameterizing hydrodynamics in a 30 km scale to larger regional and national scale models. Currently, riverbed hydrostatic pressure, dynamic pressure, and shear stress are three commonly recognized bed conditions that affect HEFs, RTDs, and the multiscale feedback among HBGC. This section focuses on the control mechanisms of these conditions under diverse spatial and temporal scales. For convenience, we represent hydrostatic pressure and dynamic pressure as water depth and dynamic pressure head. In addition, we further divide the diverse topographic features as spanwise and streamwise geometric fea-

tures, which are quantified by a spanwise coordinate s_t and a streamwise coordinate s_L, respectively. Here s_L is defined as the distance from the first point on the river centerline to any downstream point along the centerline (red solid line in Figure 9a), and s_t is defined as the distance away from the centerline along a line perpendicular to the centerline (see perpendicular lines in Figure S6). For convenience, a negative sign is used if a location is to the left bank of the river centerline as shown in Figure 9a.

3.5.1 Spanwise geometric structure

Figure 9b shows that variations of bed elevation, water depth, bed shear stress, and bed dynamic pressure head along the spanwise coordinate s_t. It is observed that the water depth shows a reversed shape compared to that of the bed elevation. This can be explained by the difference between WSE and bed elevation and WSE is approximately constant at a cross section. This also means the water depth is largely determined by the cross-sectional shape of riverbed geometry. For the bed shear stress, we observe the distribution is similar to the water depth distribution, though that shows more locally maximum/minimum variations. This suggests that bed shear stress is not only controlled by cross-sectional shape but also local features. For the dynamic pressure head, there is no obvious relationship to the riverbed cross-sectional shape but it randomly varies along the spanwise coordinate. This suggests the dynamic pressure head is likely determined by geometric features uniformly distributed on the cross section. Though not compared to the dynamic pressure measured in field surveys, such an implication can be proved by the work of Chen et al. (2019) in which the dynamic pressure on a streambed with mm scale resolution is directly resolved. As shown, the water-worked streambed has a close-Gaussian distribution (see Figure S7a) and Kirchner et al. (1990); Nikora et al. (1998)) and generates a dynamic pressure approximately randomly distributed on the riverbed (Figure S7b,c), and along spanwise (Figure S7e) and streamwise (Figure S7f) directions. For the geometry considered here, only the size of rough elements shows an approximately uniform feature and therefore it is reasonable to attribute the random dynamic pressure head to size and distribution of rough elements. Similarly, the local variations in bed shear stress are also likely attributed to the local rough elements because a close-Gaussian distribution of roughness elements contributes to a near-Gaussian shear stress, although river slope tends to change the normal distribution (Monsalve et al., 2017).

Based on the analyses of the geometric feature and the distribution of dynamic conditions, two sets of parameters are defined to quantitatively study the connection of geometric feature and characteristic behaviors of bed conditions on each cross section. The first set of parameters includes the locations of bathymetry minimum ($\vec{x}_{bm}$), water depth maximum ($\vec{x}_{dm}$), and bed shear stress maximum ($\vec{x}_{sm}$). The second set of parameters includes the maximum water depth (h_m), maximum bed shear stress (τ_m), and cross-sectional average dynamic pressure head (h_{da}). Here the bed shear stress is defined as $\tau_{xy} = \sqrt{\tau_x^2 + \tau_y^2}$ and τ_m is the maximum τ_{xy} at each cross section.

Figure 9a,b shows these newly defined locations on the riverbed and cross section A. The result shows that the location of water depth maximum almost overlaps with the location of bathymetry minimum for most cross sections (see black and green dots in Figure S8), which suggests that locations of maximum water depth on each cross section are controlled by riverbed geometric structure. By contrast, most of the locations of maximum bed shear stress overlap with locations of bathymetry minimum in the half upstream region ($x < 10$ km), but show obvious deviations in the half downstream region ($x > 10$ km). This suggests that bed shear stress in the upstream is more likely controlled by riverbed geometry, but in the downstream likely controlled by both riverbed geometry and local geometric features. Such a difference may be attributed to the redistribution of flow velocity (and water depth) in the downstream where large bars and islands are more frequently observed than in the upstream. Despite the complex local distribution, the value of water depth and bed shear stress fall in the range of [0, h_m] and [0, τ_m] with h_m = 13.02 m and τ_m = 30.34 N/m^2, respectively. For the dynamic pressure head, we observe that it varies between 0 to $2h_{da}$, with an average value of h_{da} = -0.33 m. Similar behaviors in water depth, bed shear stress, and dynamic pressure head can also be observed on other cross sections (Figure 9c,d). The characteristic values for water depth (h_m), bed shear stress (τ_m), and dynamic pressure head (h_{da}) are 11.45 m, 17.92 N/m^2, and -0.34 m on cross-section B; and 10.24 m, 22.38 N/m^2, and -0.29 m on cross-section C. These results show that characteristic water depth and bed shear stress all vary along the river centerline, though water depth and bed shear stress fall in the range of [0, h_m] and [0, τ_m] on the three cross sections. The dynamic pressure, however, shows little variations along the river centerline, which is similar to the dynamic pressure from fully resolved CFD models over realistic streambeds (see Figure S7 and Chen et al. (2019)). This further suggests that riverbed dynamic pressure is likely controlled

by a geometric feature uniform everywhere, i.e., close Gaussian distribution, such as roughness.

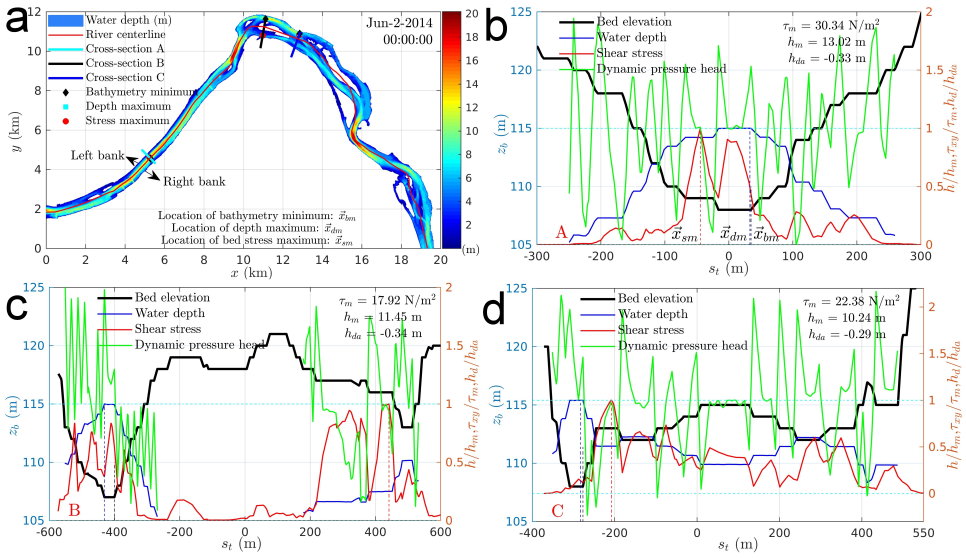

Figure 9. A typical distribution of water depth, a centerline defined from the spatial range of the water depth, and three example cross sections perpendicular to the centerline (a). Variations of bed elevation, normalized water depth (h/h_m), normalized bed shear stress (τ_{xy}/τ_m), and normalized bed dynamic pressure head (h_d/h_{da}) along the spanwise coordinate at three cross sections (b-d).

3.5.2 Streamwise geometric structure

Section 3.5.1 shows that characteristic water depth and bed shear stress vary along river centerline but dynamic pressure head does not; however, these results are based on three cross sections at one flow rate. To further study these observations at more cross sections and their dependence on flow rate, Figure 10 shows the variations of characteristic water depth (cross-sectional maximum water depth h_m), bed shear stress (cross-sectional maximum stress τ_m), and dynamic pressure head (cross-sectional average dynamic pressure head h_{da}) along the streamwise coordinate at low flow (T2) and high flow (T1 and T3) scenarios. It is observed that characteristic water depth and bed shear stress vary with both flow rate and the streamwise coordinate. Compared to bed shear stress, the variation of water depth shows more obvious dependence on the falling and rising feature in the riverbed elevation as the zig-zag (discontinuity) feature is generated from

riverbed geometry. The bed shear stress, also showing its dependence on the falling and rising feature in the bed elevation, is smoother along the river centerline. Such a difference suggests that water depth is mainly controlled by riverbed geometric feature, but shear stress is controlled by both geometric features and dynamic local flow conditions. Further, Figure 10c shows that dynamic pressure head varies between -0.4 m $\sim$ -0.3 m with an average value -0.35 m for all flow rate and most locations, which means that the dynamic pressure head is not strongly affected by flow rate and its value is approximately uniform along the river centerline. This further implies that the dynamic pressure head is more likely induced by locally uniform flow conditions such as small-scale turbulence generated from flow separation induced by small scale roughness (Hardy et al., 2010; Chen et al., 2019; Kim et al., 2020). For the river section considered here, Figure S9a,b shows the size of the vortex structure quantified by λ_2 (Jeong & Hussain, 1995) is approximately uniform despite very different topographic features along the river. This phenomenon can also be observed in a previous CFD modeling (Chen et al., 2019) where the vortex structure near the streambed has similar size as shown in Figure S9c. Such a work also shows that the vortex structure far away from the streambed is obviously different from that near the bed (Figure S9d).

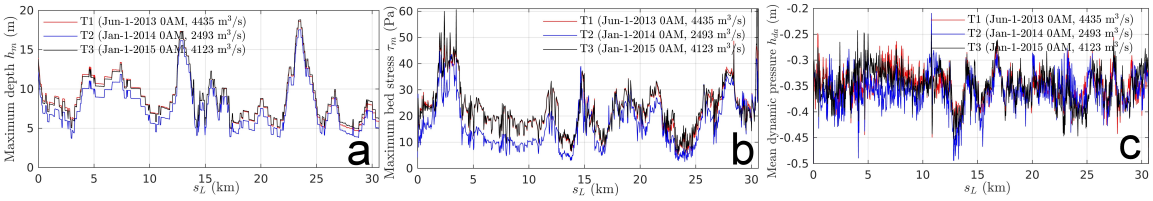

Figure 10. The variations of characteristic water depth (a), bed shear stress (b), and dynamic pressure head (c) along the streamwise coordinate (s_L) at low flow (T2) and high flow (T1 and T3) scenarios.

3.5.3 Discharge variations

To further study the effects of discharge on characteristic water depth, bed shear stress, and dynamic pressure head, Figure 11a,b,c shows variations of these values with respect to time during 2013-2015 at three locations (s_L = 3 km, 12.3 km, and 24 km, see X1 - X3 in Figure 12). The result indicates that water depth and bed shear stress vary with time at the three locations. The dynamic pressure head, although also vary-

ing with time, shows a variation range -0.45 m $\sim$ -0.35 m at the three locations over the 3 years. This suggests the dynamic pressure head is likely little affected by flow rate.

To further investigate the role of flow rate in affecting characteristic water depth and bed shear stress, Figure 11d,e shows the relationship between their values with respect to discharge in a log-log scale. It is observed that water depth is determined by flow rate through $h_m = aQ^b$. Though this relationship is obtained from data fitting, the high R^2 (0.85 $\sim$ 0.99 at X1 - X3) implies that such a relationship is reliable. Figure 11f (red circle) also shows the R^2 at all cross sections using the same formula for data fitting. Though the R^2 reduces from 0.99 at the inlet to 0.75 to the outlet, this value still suggests that water depth is directly affected by flow rate through $h_m = aQ^b$. Here the fitting parameter a reflects the effect of streamwise slope and b reflects the effects of cross-sectional shape (see variations of a and b along centerline in Figure S10). The similar data-fitting method is also applied for the bed shear stress as shown in Figure 11e. The result indicates that bed shear stress can be well represented using $\tau_m = aQ^b$ at some locations, but has larger uncertainty in other locations (Figure 11f blue cross). More specifically, the fitted R^2 is larger than 0.9 for most locations in the half upstream ($s_L < 15$ km), but could be reduced to 0 in the half downstream ($s_L > 15$ km). This suggests that bed shear stress in the half upstream is likely mainly controlled by flow rate, streamwise slope, and cross-sectional shape, but may be further affected by other local features in the downstream. For example, the islands in the regions near cross-sections B and C (the white regions between 10 km and 13 km in Figure 9a or 15 km and 20 km in Figure 11f) divert the flow into two channels and create two locally maximum bed shear stress, which invalidates the relationship between shear stress and flow rate applicable for upstream regions with only one channel. These combined effects from flow rate and large and local scale geometric features result in the complex distribution of bed shear stress in the downstream region.

4 Discussion

4.1 Roughness quantification

It is long recognized that hydraulic roughness estimation is the primary uncertainty of numerical modeling of natural rivers (USACE, 1994). The hydraulic roughness is a parameter used to estimate the resistance applied to flow from complex sediment struc-

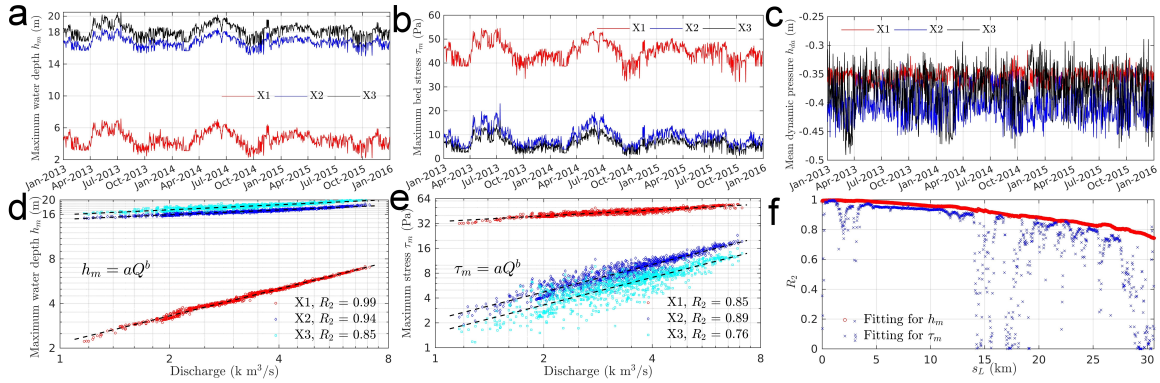

Figure 11. Variations of characteristic water depth (a), bed shear stress (b), and dynamic pressure (c) with respect to time at three locations. (d-e) Variations of characteristic water depth and bed shear stress with respect to discharge. (f) Variation of R^2 of data fitting along the river centerline.

tures, e.g., sand, gravels, pebbles, and boulders, and other in-stream structures such as vegetation and large-woody debris. Accurate estimation of hydraulic roughness in natural environments requires high-resolution measurements of the in-stream sediment structure; however, most airborne methods such as LiDAR cannot efficiently measure the detailed structure of individual sediment ranging from mm to dm. Grain size distribution surveys based on manual sediment counts provide a reliable way to estimate grain size but not applicable for tens of kilometers scale rivers with deep water. Therefore, though important for numerical modeling, roughness estimation for large-scale rivers with deep water is still a challenging problem. For the purposes of providing roughness estimation for large-scale river modeling, we give a brief discussion of three roughness estimation methods and associated modeling uncertainty.

4.1.1 Calibration with observations

Roughness calibration with observed water stage is an efficient approach for roughness estimation in 3D free-surface models. The physical basis for this approach is that the bulk flow velocity in streams is monotonically related to bed roughness and therefore an optimal roughness can be obtained by monotonically adjusting a roughness parameter to match modeled WSE with observed ones. Usually, a very small roughness height, e.g., 0, results in an underestimation of WSE; while a high roughness height, e.g., the size of the biggest sediment, results in an overestimation of WSE. With this in mind, a

series of numerical experiments can be designed by systemically adjusting the roughness parameter from 0 to the biggest value and the relative error between modeled WSE and observed ones can be directly calculated as shown in Figure 3b. An optimal roughness parameter for each observation location can be obtained, which is here referred to as a locally optimal roughness height.

However, as the roughness parameter calibrated in this way usually works well for a single location, this means that applying such a parameter to all locations cannot guarantee overall modeling accuracy for all locations. Different strategies can be applied to solve this problem. The simplest strategy is to choose one roughness parameter and apply it uniformly to the whole domain. Such a parameter can be directly identified from error diagrams (Figure 3b or Figure S2), which has a value of $k_s^1 = 12.2$ cm. Using this strategy, the overall modeling accuracy is about -30 cm $\sim$ 30 cm and 7.5 cm $\sim$ 30 cm in terms of ME and MAE (see OFK1 in Table 1). The second strategy is to decompose the riverbed into two regions with different roughness parameters assigned to each region. This strategy is based on the fact that the error diagrams (Figure 3b or Figure S2) show two different behaviors at the region 100B and other five locations. Following this concept, $k_s^{2b} = 25.56$ cm is assigned for the region at 100B and $k_s^{2a} = 6.25$ cm is assigned for all other regions. The overall modeling accuracy for WSE using such a strategy is about -17 cm $\sim$ 15 cm and 9 cm $\sim$ 15 cm in terms of ME and MAE (see OFK2 in Table 1). Adjusting the spatial range of region at 100B improves a little of the accuracy (see OFK2R in Table 1). Overall, we see that the modeling accuracy of using one-ks and two-ks strategies is $\pm$ 0.3 m and $\pm$ 0.15 m in terms of ME, and 0.3 m and 0.15 m in terms of MAE. It is important to mention that such modeling accuracy can be roughly predicted using error diagrams without running actual simulations (cases OFK1 and OFK2 in Table 1). This means that the error diagram is a good tool for designing calibration strategy. We also tested the strategy of interpolating the locally optimal roughness height to 50 uniformly distributed regions (see k_s and regions in Figure S3). The overall accuracy for WSE is -19.4 cm $\sim$ 8.5 cm and 9.3 cm $\sim$ 19.4 cm in terms of ME and MAE (case OFK50 in Table 1), respectively. This result suggests that interpolating the locally optimal roughness height to more regions does not improve modeling accuracy because interpolating itself may introduce extra error to the roughness field. From the above discussion, we identify that the best strategy is to decompose the riverbed into N regions with N equal to the number of survey locations. Without further adjustment of rough-

ness parameter, such a strategy gives an overall modeling accuracy of WSE as -16.5 cm $\sim$ 6.4 cm and 7.6 cm $\sim$ 19.6 cm in terms ME and MAE, respectively.

To further improve the modeling accuracy, local adjustment of the roughness parameters is necessary. This is because the locally optimal roughness parameters neglect the flow interactions due to locally variable flow resistance, backwater effects from downstream to upstream, and the effects of sinuosity. The local adjustment is used to incorporate these effects into the calibration and achieve a globally optimal roughness calibration. As higher uncertainty (case OF0 in Table 1) occurs at the upstream locations (100B, 100N, and 100D) using the locally optimal roughness height, we systematically adjust the roughness parameters at these locations. The final modeling accuracy for WSE is -7.5 cm $\sim$ 6.4 cm and 7.5 cm $\sim$ 12.7 cm in terms of ME and MAE, respectively. Further improvement of the accuracy is possible but not necessary as the relative errors to water depth have been reduced to -2.7% $\sim$ 2.1% and 2.1% $\sim$ 5.3% in terms of ME and MAE. Nevertheless, it is worth summarizing how local adjustment improves modeling accuracy. Firstly, increasing roughness height at the most upstream location (100B) improves the accuracy of WSE only at that location (see OF0, OF1, and OF2 in Table 1); secondly, changing roughness height at 100N has little effects on WSE at 100N and neighbouring upstream locations (see OF2 and OF3 in Table 1); and thirdly, increasing roughness height at 100D significantly affects WSE at all upstream locations and has a larger influence on the locations closer to that location. These results suggest that roughness heights at some critical locations (most upstream and close to pool) have a larger impact on the overall modeling accuracy.

4.1.2 Converted from Manning's coefficient

The roughness calibration method discussed in Section 4.1.1 can be applied for any rivers where WSE observation is available but is usually time-consuming. 1D and 2D models have been widely used to predict WSE and Manning's coefficient has been available in these models. For example, for the river section studied in this work, the calibrated Manning's coefficients from a 2D CFD model are 0.038, 0.035, 0.034, 0.027, 0.027, and 0.03 at 100B, 100N, 100D, LI, 100H, and 100F (Niehus et al., 2014). In these situations, the roughness parameter required in 3D CFD models can be directly converted from well-calibrated Manning's coefficient based on a force balance at the riverbed. Specifically, the force balance can be described as $\tau_b = \rho g S R = 1/8 f \rho U^2$ with τ_b, S, R, f, and U

denoting average bed shear stress, channel slope, hydraulic radius, Darcy-Weisbach friction factor, and average streamwise velocity. For gravel bed rivers, it was shown that $\sqrt{\frac{8}{f}} = a(\frac{R}{k_s})^b$ with $b = 1/6$ and a has a value of 6.7, 7.3, 8.2, 8.4, 9.39, etc. when $R/k_s > 10$ (Chaudhry, 2008; Rickenmann & Recking, 2011; Ferguson, 2013). Meanwhile, the Manning's equation shows $U = \frac{1}{n}R^{2/3}S^{1/2}$ with n denoting the Manning's coefficient. Using these formulas, the relationship between n and k_s can be quantified as $n = \frac{1}{a\sqrt{g}}k_s^{1/6}$ if k_s has a unit of foot or $n = \frac{1.219}{a\sqrt{g}}k_s^{1/6}$ if k_s is in SI unit. The coefficient a characterizes the type of sediment that requires further calibration, however could use an average value of 8.0 for a rough estimation of k_s. In this work, as the locally optimal roughness height can be deterministically calculated and the modeled WSE at 100F gives a very good accuracy (see 100F in OF0 Table 1), we back-calculated the value of $a = 8.4$ using $k_s = 7.42$ cm $= 0.2434$ ft and $n = 0.03$. With the calibrated value for a, hydraulic roughness k_s can be converted as shown in case MS in Table 1. The modeling accuracy of WSE using these roughness parameters is -4.7 cm $\sim$ 7.7 cm and 6.4 cm $\sim$ 13.9 cm in terms of ME and MAE, respectively. This result suggests that the roughness height converted from the well-calibrated Manning's coefficients of 2D models can give similar modeling accuracy compared to using the globally optimal roughness height. Further local adjustment of these roughness parameters does not significantly improve modeling accuracy (see MS2 and MS3 in Table 1).

4.1.3 Estimated from microtopography

Both roughness calibration and conversion from the Manning's coefficients require observation of water stage and these calibrations may not guarantee the accuracy of other flow quantities such as pressure, flow velocity, and bed shear stress. A more accurate and physics-based method for evaluating the effects of bed roughness is to directly resolve the influence of microtopography on flow dynamics. However, the success of such a method depends on high-resolution measurements of riverbed microtopography, computational techniques to deal with complex geometry in CFD codes, and available high-performance computing resources. Owing to the rapid development of structure-from-motion (SfM) photogrammetry and unnamed aerial vehicles, remote sensing of riverbed sediment structure with 1 cm $\sim$ 5 cm resolution over a 40-kilometer river reach has been possible (Carr et al., 2019). This data can be used either for quantifying locally distributed grain size distribution or used as a geometric boundary for 3D CFD models where the effects of

sediment structure on flow dynamics can be directly resolved. At the patch scale (a few meters to tens meters), SfM photogrammetry-scanned high-resolution (mm - cm scale) riverbeds have been used to directly resolve the effects of sediment structure on the flow resistance (Chen et al., 2018, 2019). A quantitative relationship has been identified between hydraulic roughness, turbulent vortex structure, and characteristic sediment size. Therefore, with available high-resolution riverbed structure from SfM and previous theory on hydraulic roughness, the distributed hydraulic roughness height in large rivers can be directly estimated and the surface decomposition approach developed in this work can be used to generate distributed roughness for the CFD code.

4.2 Effects of discharge and spatial variations on bed conditions

Section 3.5 discusses the effects of spatial heterogeneity and discharge variations on bed conditions but is limited to a few selective times and locations. Figure 12 shows the spatial (horizontal axes) and temporal (vertical axes) maps of cross-sectional minimum bed elevation, maximum water depth, maximum bed shear stress, and average bed dynamic pressure head. The spatial and temporal range is 30 km and 2013-2015 with a spatial resolution of 30 m (1001 points) and temporal resolution of 1 day (1094 dates). As the riverbed bathymetry does not evolve with time, we observe that minimum bed elevation does not change along the vertical coordinate (time), but only varies along the streamwise coordinate (s_L). Here X1, X2, and X3 denote locations with the highest, second lowest, and lowest bed elevation, respectively. T1, T2, and T3 denote 0AM on 01 June 2013, 01 January 2014, and 01 January 2015, respectively.

Moving to the map of water depth (Figure 12b), it is observed that regions with yellow color in Figure 12a are filled with blue color and vice versa for the regions with blue color in Figure 12b. For example, water depth at X1 shows yellow color on Figure 12a but appears as deep blue color in Figure 12b; at X2 and X3 is a deep blue color on Figure 12a but shows yellow color on Figure 12b. In addition, Figure 12b shows that regions with yellow color always show yellow color and regions with deep blue always show deep blue color along the vertical direction. These results agree with previous understanding that water depth is inversely related to the bed elevation and suggest the spatial structure of water depth varies little with time (or flow rate). Figure 12b also shows that water depth varies with time (see color changes along vertical direction in the regions between 3 km and 9 km) though such a variation is not considerable compared to the changes

along centerline (more obvious color change). The probability density function (pdf) analysis over all spatial coordinates and all dates shows that water depth is strongly affected by the discontinuous changes (periodicity) of bed elevation along the streamwise direction (Figure 13a). Such a pdf also shows that 50% of water depth is less than 7.85 m and 75% of water depth is less than 10 m during the 3-year period.

Moving to the map of bed shear stress (Figure 12c), it is observed that larger variations appear along the vertical direction compared to those in water depth and the regions with yellow color approximately correspond to the regions with yellow color on Figure 12a. This suggests that bed shear stress varies with both time (flow rate) and the bed elevation changes along river centerline. In addition, the obvious color changes along horizontal and vertical direction mean that both variations in flow rate and streamwise geometric feature dominate the distribution of bed shear stress. To further understand the control mechanisms of bed shear stress, Figure 13b show the probability density function of bed shear stress. The result shows that such a pdf has a similar shape to water depth, but removes the discontinuous (periodic) behavior as in the water depth. This can be explained by the fact that bed shear stress is affected by both streamwise topographic features and more uniformly distributed small-scale turbulence from flow separation (Hardy et al., 2010). Though the streamwise topographic feature is discontinuous, the turbulent flows contributing to bed shear stress have a much smaller scale than the topographic scales and thus contribute to a much smoother pdf distribution. For example, though with large bed forms and protruding grains, the pdfs of the bed shear stress on these streambeds still behave like smooth Gaussian distribution at small river slope (Monsalve et al., 2017). This work also shows that a large river slope results in a skewed pdf in bed shear stress, which explains the positive skewness in the bed shear stress as the river section studied has large variations in river slope, i.e., the bed elevation change along the centerline. In addition, the pdf shows that average bed shear stress is 20 N/m^2 and 90% of bed shear stress falls in the range between 5 N/m^2 and 35 N/m^2. This means that bed shear stress may initiate the motions of riverbed sediments with a particle size less than fine gravel (4 mm $\sim$ 8 mm) because 90% of the predicted shear stress is higher than the critical shear stress of fine gravel (Berenbrock & Tranmer, 2008). This may significantly affect the chemical and biological processes associated with sediments less than 1 cm.

For the cross-sectional average dynamic pressure head, Figure 12d shows it varies a little along the streamwise locations and time. Using the values of dynamic pressure head, Figure 13c shows the probability density function of the cross-sectional average dynamic pressure head. The result shows that the distribution is similar to a normal distribution (red curve in Figure 12c) with a mean and standard deviation as -0.353 m and 0.0352 m, respectively. Such a similarity to a normal distribution suggests the cross-sectional average dynamic pressure head is likely a randomly distributed field. Such an implication may be further demonstrated by a randomly distributed dynamic pressure and its close-Gaussian distribution from a roughness fully resolved CFD modeling (Figure S7 and Chen et al. (2019)). Figure 13c also shows that the pdf of dynamic pressure head does not display any feature similar to that of water depth and bed shear stress, which suggests that dynamic pressure is not affected by the streamwise geometric feature. Figure 13c also shows that 95% of the dynamic pressure falls in the range -0.42 m $\sim$ -0.28 m, which is equivalent to the range $\mu \pm 2\sigma$.

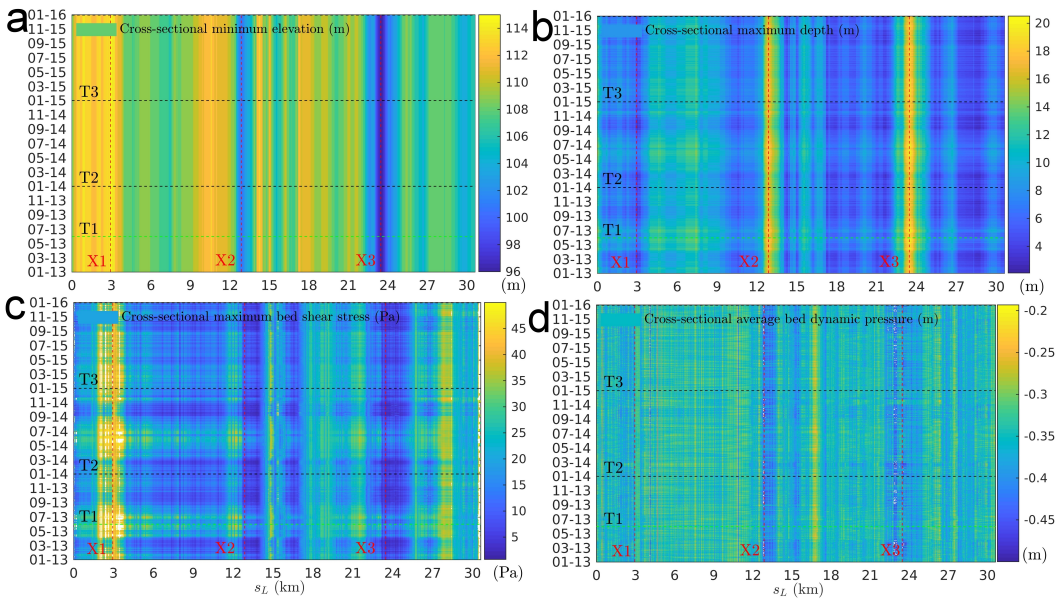

Figure 12. The spatial (s_L) and temporal (date) maps of river cross-sectional minimum elevation (a), maximum water depth (b), maximum bed shear stress (c), and bed dynamic pressure (d). X1 - X3 and T1 - T3 are three selective locations and dates used to illustrate the variation details of bed conditions. White spots on each figure denote values outside the range as shown on the color bars.

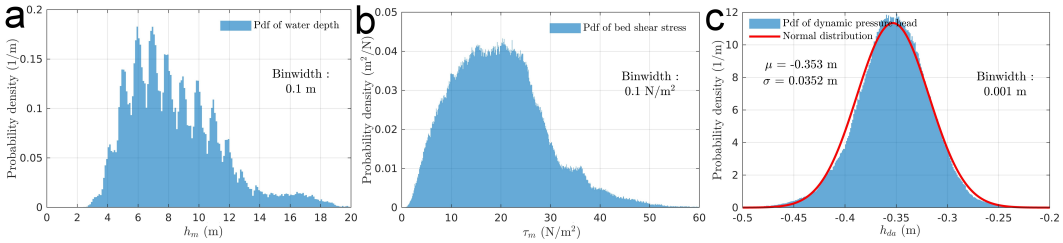

Figure 13. The pdf of cross-sectional maximum water depth (a), maximum bed shear stress (b), and average dynamic pressure head (c) over all streamwise coordinates and dates.

4.3 Computational efficiency

Despite the rapid growth in computational capacity in the past two decades, it is still a bottleneck for CFD modeling of natural rivers with tens of kilometer scale over a couple of years. However, we show that such a limitation may be relieved using highly efficient CFD code, spatiotemporal decomposition approach, and a few hundred CPUs commonly available in university-scale or national-scale cyberinfrastructure. The discussion here is based on modeling results during short-term 2011 (1 month), 2013-2015 (36 months), and 2018-2019 (22 months) by using Cascade, a high-performance computer managed by the Environmental Molecular Sciences Laboratory (EMSL) at PNNL (www.emsl.pnnl.gov). For convenience, we define CPU time and solution time as the time consumed by computers and the time of water flow in the CFD model, respectively. The computational efficiency can be further quantified by the ratio of solution time and CPU time.

Figure 14 shows the advancement of solution time with respect to CPU time for the short-term medium flow case. It is observed that the computational efficiency increases linearly with increasing time step ΔT (solid lines with $N_p = 256$). In addition, increasing the number of processors from 256 to 512 only increases the computational efficiency by 1.5 times. Further increasing the number of processors decreases the computational efficiency, which means that an optimal number of processors exists for our model. The computational efficiency is also affected by the selection of linear solve; in our case, PCG solver with DIC conditioner increases the computational efficiency by 3.6 times compared to using a generalised geometric-algebraic multigrid (GAMG) solver. Despite the changes of time step and number of processors, modeled WSE does not change (see Figure S4). Following such an analysis, we show that the computational efficiency is around 36 by using 512 processors, 3 s as the time step, and DIC-PCG as the linear solver. This means

we can simulate 1 month solution time in less than one day of wall-clock time or 1 day solution time in 40 minutes (1/36 days) of wall-clock time. With the same parallel computation setups, we divide simulations during medium-term and long-term into 36 and 22 cases and run all cases simultaneously (see details in Section 2.6). The CFD code log files show that all simulations were completed in less than 6 days of wall-clock time. Considering the number of processors, the total CPU hours spent is about 1.1 million, which is equivalent to 19,000 CPU hours for each month. Note that the time considered here does not include the computational time used for calibration; however, our work shows that calibration is only required once. Therefore, for rapid predictions of the streamflow with well-calibrated roughness parameters, the computational efficiency may be feasible in terms of how much time and how many CPU hours are required.

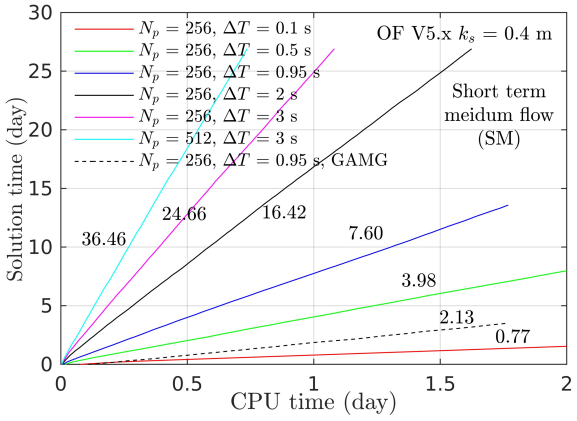

Figure 14. The advancement of solution time with respect to CPU time. N_p and ΔT denote the number of processors and time step. Linear solver used for solid lines is DIC-PCG and the dashed line is GAMG.

4.4 Implications for biogeochemistry, subsurface models, and field investigations

The long-term goal of river corridor research is to develop accurate and efficient predictive models for water quality, nutrient dynamics, and ecosystem health. The success depends on four aspects: multiprocess coupling between hydrodynamics and biogeochemistry; multidomain coupling among streamwater, hyporheic zone, and groundwater; reducing model uncertainty based on improved field measurements; and develop-

ing efficient computational framework. As we discussed the computational efficiency in Section 4.3, we now focus on the other three aspects.

First, the multiprocess coupling is important because flow dynamics and turbulence directly control fine-scale sediment and chemicals transport (Ongley, 1996; Venditti et al., 2010; Yang & Nepf, 2018) and dissolved oxygen concentration and mass transfer rate of respiration (Grant, Azizian, et al., 2018); and indirectly affect the population and distribution of small microbes and large aquatic fish and vegetation by controlling oxygen concentration and aerobic/anaerobic respiration. Within the framework presented in this work, transport of fine sediments, chemicals, and oxygen; chemical reactions of aerobic and anaerobic respiration (Li et al., 2020); and microbial community growth using continual or discrete population balance model (Song et al., 2014) can all be fitted into a comprehensive multiprocess model. Such a comprehensive model can then be applied to study individual HBGC processes and their interactions in a more realistic river corridor environment.

Second, the multidomain coupling among streamwater, hyporheic zone, and groundwater is important. This is because the characteristic spatial and temporal scales in each zone are very different and thus resolving all scales in a single model is not practical due to limited data and high computational costs. Instead, each domain is usually separately modeled and then coupled together using either one-way coupling or fully coupling techniques (Cardenas & Wilson, 2007; Maxwell et al., 2014; Bao et al., 2018; Li et al., 2020). For example, the streamwater is usually modeled with the 1D Saint-Venant equations or the 2D shallow water equations and the groundwater is modeled with Richards equations together with other solute transport models. The coupling between the streamwater and groundwater is through imposing continuous fluxes of water or solutes at the interface between the two domains. In one-way coupling models, the riverbed total pressure from the streamwater, a summation of hydrostatic pressure and dynamics pressure, from the streamwater is usually required as a pressure boundary condition for the subsurface model. However, the dynamic pressure cannot be well predicted without using 3D CFD models with a good estimation of bed roughness. The present work thus provides a solution for efficient prediction of dynamic pressure for large-scale natural rivers, which further reduces the boundary condition uncertainty for subsurface models.

Despite reducing uncertainties for subsurface models and improving understanding of riverbed biogeochemistry, our model may also help in designing field investigations. For example, the spatiotemporal maps of water depth, bed shear stress, and dynamic pressure provide direct information of where and when these quantities are important. As dynamic pressure and bed shear stress are further tied to mass fluxes of water, oxygen, and carbon, these maps can further provide information for where HEFs, chemical reactions, or microbial activities may be important. As our model enables predictions of flow dynamics at all spatial locations and all dates, it also enables direct comparisons between model results with field measurements at all individual locations and time periods. This provides a direct approach for data-model integration that can improve both modeling accuracy and field survey quality (Scheibe et al., 2018; Schilling et al., 2019).

5 Conclusions

This work proposed a semi-automated workflow that combines topographic and water stage surveys, 3D computational fluid dynamics modeling, distributed rough wall resistance modeling, and spatiotemporal decomposition to simulate the streamflow in a 30-kilometer-long river reach in the Columbia River spanning 9 years. Specifically, a LiDAR measured river topography is represented by a zig-zag grid in the 3D model. The effect of geometric differences between an actual riverbed and the computational mesh on streamflow is modeled with a distributed rough wall resistance model with the roughness parameters calibrated with measured WSE at six locations during 2011. The insignificant time-history effect on WSE enables decomposing the simulation period 2013-2015 into 36 months and 2018-2019 into 22 months with each month simulated simultaneously using parallel computation.

Systematical roughness calibration shows that the distributed roughness field enables an average WSE difference between modeled and observed ones as -7.5 cm $\sim$ 6.4 cm, which is equivalent to -2.7% $\sim$ 2.1% relative to average water depth. With this calibrated roughness field, the modeling accuracy for WSE is reported as -15.6 cm $\sim$ 9.1 cm, -14.4 cm, and 7.2 cm for short-term, medium-term, and long-term predictions; while is equivalent to -7.1% $\sim$ 6.6%, -4.6%, and 5.4% relative to the average water depth.

Using the validated modeling results, the dependencies of riverbed hydrodynamic conditions on flow rate temporal non-stationarity and bathymetry spatial heterogene-

ity are further investigated. It is found that hydrodynamic pressure is randomly distributed across the riverbed over all times, which is further linked to a normal distribution; the riverbed hydrostatic pressure is controlled by flow rate and large geomorphic features such as streamwise slope and cross-sectional shape, whose probability density function reflects the discontinuous feature of the bed elevation along the river centerline; and the bed shear stress is controlled by flow rate and large and small topographic features with its probability function showing a similarity to that of both water depth and dynamic pressure. Further computational efficiency analyses show that the time step, number of processors, selection of linear solver, and IO affect the final computational efficiency. Using the spatiotemporal decomposition, 3D CFD modeling the streamflow in 58 months can be achieved in less than six days and using 1.1 million CPU hours.

Given the high modeling accuracy and computational efficiency of our model, this work provides a generic framework with the potential to enable process coupling between hydrodynamics and biogeochemistry, domain coupling between streamwater and groundwater, and direct data-model integration, all of which contribute to more accurate and efficient predictive models for river corridor systems.

Acknowledgments

This research was supported by the United States Department of Energy (DOE) Office of Biological and Environmental Research (BER), Subsurface Biogeochemical Research program, through the PNNL Subsurface Science Scientific Focus Area (SFA) project (http://sbrsfa.pnnl.gov/). PNNL is operated for the DOE by Battelle Memorial Institute under Contract No. DE-AC05-76RL01830. Data and modeling products are retained in the SFA data management system and are available from the authors on request. The high-performance computation resources were provided by EMSL Cascade.

Data availability

OpenFOAM setups, data, and Matlab code are available at Velo (sbrsfa.velo.pnnl.gov), a customizable, reusable and collaborative knowledge management system at PNNL.

References

Bao, J., Zhou, T., Huang, M., Hou, Z., Perkins, W., Harding, S., ... Zachara, J. (2018). Modulating factors of hydrologic exchanges in a large-scale river reach:

Insights from three-dimensional computational fluid dynamics simulations. *Hydrological Processes*, *32*(23), 3446–3463. doi: 10.1002/hyp.13266

Battin, T. J., & Sengschmitt, D. (1999). Linking sediment biofilms, hydrodynamics, and river bed clogging: evidence from a large river. *Microbial Ecology*, *37*(3), 185–196. doi: 10.1007/s002489900142

Berenbrock, C., & Tranmer, A. W. (2008). Simulation of flow, sediment transport, and sediment mobility of the Lower Coeur d'Alene River, Idaho. *USGS Scientific Investigations Report*(2008-5093), 164.

Blocken, B., Stathopoulos, T., & Carmeliet, J. (2007). CFD simulation of the atmospheric boundary layer: wall function problems. *Atmospheric Environment*, *41*(2), 238–252. doi: 10.1016/j.atmosenv.2006.08.019

Boano, F., Harvey, J. W., Marion, A., Packman, A. I., Revelli, R., Ridolfi, L., & Wörman, A. (2014). Hyporheic flow and transport processes: mechanisms, models, and biogeochemical implications. *Reviews of Geophysics*, *52*(4), 603–679. doi: 10.1002/2012RG000417

Cardenas, M. B., & Wilson, J. L. (2007). Hydrodynamics of coupled flow above and below a sediment-water interface with triangular bedforms. *Advances in Water Resources*, *30*(3), 301–313. doi: 10.1016/j.advwatres.2006.06.009

Carr, J. C., DiBiase, R. A., & Yeh, E. C. (2019). Geomorphic and structural mapping for remote bedrock river corridors in the Taiwan Central Range using paired outcrop and kilometer scale UAV surveys. In *Gsa annual meeting.* Phoenix, Arizona, USA. doi: 10.1130/abs/2019AM-335826

CFDDirect. (2017). *OpenFOAM-5.x: free open source CFD.* http://www.OpenFoam.org.

Chaudhry, M. H. (2008). *Open-Channel Flow* (2nd ed.). Springer US. doi: 10.1007/978-0-387-68648-6

Chen, Y., DiBiase, R. A., McCarroll, N., & Liu, X. (2019). Quantifying flow resistance in mountain streams using computational fluid dynamics modeling over structure-from-motion photogrammetry-derived microtopography. *Earth Surface Processes and Landforms*, *44*(10), 1973–1987. doi: 10.1002/esp.4624

Chen, Y., Liu, X., Gulley, J. D., & Mankoff, K. D. (2018). Subglacial conduit roughness: insights from computational fluid dynamics models. *Geophysical Research Letters*, *45*(20), 11206–11218. doi: 10.1029/2018GL079590

Deshpande, S. S., Anumolu, L., & Trujillo, M. F. (2012). Evaluating the performance of the two-phase flow solver interFoam. *Computational Science & Discovery*, *5*(1), 014016. doi: 10.1088/1749-4699/5/1/014016

Ferguson, R. (2013). Reach-scale flow resistance. In *Treatise on geomorphology* (Vol. 9, pp. 50–68). doi: 10.1016/B978-0-12-374739-6.00230-X

Goyal, M. R. (2014). *Sustainable micro irrigation: principles and practices* (1st ed.; Megh R. Goyal, Ed.). Waretown, NJ, USA: Apple Academic Press.

Grant, S. B., Azizian, M., Cook, P., Boano, F., & Rippy, M. A. (2018, mar). Factoring stream turbulence into global assessments of nitrogen pollution. *Science*, *359*(6381), 1266–1269. doi: 10.1126/science.aap8074

Grant, S. B., Gomez-Velez, J. D., & Ghisalberti, M. (2018). Modeling the effects of turbulence on hyporheic exchange and local-to-global nutrient processing in streams. *Water Resources Research*, *54*, 5883–5889. doi: 10.1029/2018WR023078

Groom, J., & Friedrich, H. (2019). Spatial structure of near-bed flow properties at the grain scale. *Geomorphology*, *327*, 14–27. doi: 10.1016/j.geomorph.2018.10.013

Hardy, R. J., Best, J. L., Lane, S. N., & Carbonneau, P. E. (2010). Coherent flow structures in a depth-limited flow over a gravel surface: The influence of surface roughness. *Journal of Geophysical Research*, *115*(F3), F03006. doi: 10.1029/2009JF001416

Harvey, J. W. (2016). *Hydrologic Exchange Flows and Their Ecological Consequences in River Corridors*. Elsevier Inc. doi: 10.1016/B978-0-12-405890-3.00001-4

Hirt, C., & Nichols, B. (1981). Volume of fluid (VOF) method for the dynamics of free boundaries. *Journal of Computational Physics*, *39*(1), 201–225. doi: 10.1016/0021-9991(81)90145-5

Issa, R. I. (1985). Solution of the implicitly discretised fluid flow equations by operator-splitting. *Journal of Computational Physics*, *62*, 40–65. doi: 10.1016/0021-9991(86)90099-9

Jeong, J., & Hussain, F. (1995). On the identification of a vortex. *Journal of Fluid Mechanics*, *285*, 69–94. doi: 10.1017/S0022112095000462

Khosronejad, A., Le, T., DeWall, P., Bartelt, N., Woldeamlak, S., Yang, X., & Sotiropoulos, F. (2016). High-fidelity numerical modeling of the Upper Missis-

sippi River under extreme flood condition. *Advances in Water Resources*, *98*, 97–113. doi: 10.1016/j.advwatres.2016.10.018

Kim, T., Blois, G., Best, J. L., & Christensen, K. T. (2020). Experimental evidence of amplitude modulation in permeable-wall turbulence. *Journal of Fluid Mechanics*, *887*, A3. doi: 10.1017/jfm.2019.1027

Kirchner, J. W., Dietrich, W. E., Iseya, F., & Ikeda, H. (1990, aug). The variability of critical shear stress, friction angle, and grain protrusion in water-worked sediments. *Sedimentology*, *37*(4), 647–672. doi: 10.1111/j.1365-3091.1990.tb00627.x

Kundu, P. K., Cohen, I. M., & Dowling, D. R. (2012). *Fluid mechanics* (5th ed.). Waltham, MA, USA: Elsevier. doi: 10.1016/C2009-0-63410-3

Kuzmin, D., Möller, M., & Turek, S. (2003). Multidimensional FEM-FCT schemes for arbitrary time stepping. *International Journal for Numerical Methods in Fluids*, *42*(3), 265–295. doi: 10.1002/fld.493

Lamb, M. P., Brun, F., & Fuller, B. M. (2017). Hydrodynamics of steep streams with planar coarse-grained beds: Turbulence, flow resistance, and implications for sediment transport. *Water Resources Research*, *53*(3), 2240–2263. doi: 10.1002/2016WR019579

Li, B., Liu, X., Kaufman, M. H., Turetcaia, A., Chen, X., & Cardenas, M. B. (2020, feb). Flexible and modular simultaneous modeling of flow and reactive transport in rivers and hyporheic zones. *Water Resources Research*, *56*(2). doi: 10.1029/2019WR026528

Liu, X., Chen, Y., & Shen, C. (2016). Coupled two-dimensional surface flow and three-dimensional sub-surface flow modeling for the drainage of permeable road pavement. *Journal of Hydrologic Engineering*, *21*(12), 04016051. doi: 10.1061/(ASCE)HE.1943-5584.0001462

Maxwell, R. M., Putti, M., Meyerhoff, S., Delfs, J.-O., Ferguson, I. M., Ivanov, V., ... Sulis, M. (2014). Surface-subsurface model intercomparison: A first set of benchmark results to diagnose integrated hydrology and feedbacks. *Water Resources Research*, *50*(2), 1531–1549. doi: 10.1002/2013WR013725

Menter, F. R., Kuntz, M., & Langtry, R. (2003). Ten years of industrial experience with the SST turbulence model turbulence heat and mass transfer. In K. Hanjalic, Y. Nagano, & M. J. Tummers (Eds.), *Proceedings of the 4th international*

symposium on turbulence, heat and mass transfer (pp. 625–632). Antalya, Turkey: Begell House,.

Monsalve, A., Yager, E. M., & Schmeeckle, M. W. (2017). Effects of Bed Forms and Large Protruding Grains on Near-Bed Flow Hydraulics in Low Relative Submergence Conditions. *Journal of Geophysical Research: Earth Surface*, *122*(10), 1845–1866. doi: 10.1002/2016JF004152

Munoz, D. H., & Constantinescu, G. (2018, dec). A fully 3-D numerical model to predict flood wave propagation and assess efficiency of flood protection measures. *Advances in Water Resources*, *122*, 148–165. doi: 10.1016/j.advwatres.2018.10.014

Niehus, S., Perkins, W., & Richmond, M. (2014). *Simulation of Columbia River Hydrodynamics and Water Temperature from 1917 through 2011 in the Hanford Reach* (Tech. Rep.). Richland, WA: Battelle-Pacific Northwest Division. doi: 10.13140/RG.2.1.5146.8409

Nikora, V. I., Goring, D. G., & Biggs, B. J. F. (1998). On gravel-bed roughness characterization. *Water Resources Research*, *34*(3), 517–527. doi: 10.1029/97WR02886

Nikuradse, J. (1933). *Laws of flow in rough pipes (English translation)* (Tech. Rep.). Washington, DC, USA: National Advisory Commission for Aeronautics.

Ongley, E. (1996). Ch13: Sediment measurements. In B. Jamie & B. Richard (Eds.), *Water quality monitoring : a practical guide to the design and implementation of freshwater quality studies and monitoring programs* (1st ed., p. 400). London, U.K.: E & FN SPON.

Powell, D. M. (2014). Flow resistance in gravel-bed rivers: progress in research. *Earth-Science Reviews*, *136*, 301–338. doi: 10.1016/j.earscirev.2014.06.001

Richmond, M. C., & Perkins, W. A. (2009). Efficient calculation of dewatered and entrapped areas using hydrodynamic modeling and GIS. *Environmental Modelling and Software*, *24*(12), 1447–1456. doi: 10.1016/j.envsoft.2009.06.001

Rickenmann, D., & Recking, A. (2011). Evaluation of flow resistance in gravel-bed rivers through a large field data set. *Water Resources Research*, *47*(7), W07538. doi: 10.1029/2010WR009793

Salim, S., Pattiaratchi, C., Tinoco, R., Coco, G., Hetzel, Y., Wijeratne, S., & Jayaratne, R. (2017). The influence of turbulent bursting on sediment resuspen-

sion under unidirectional currents. *Earth Surface Dynamics*, *5*(3), 399–415. doi: 10.5194/esurf-5-399-2017

Scheibe, T., Chen, X., Stegen, J., Huang, M., Garayburu-Caruso, V., Goldman, A. E., ... Zhu, Y. (2018). Data-model integration for improved prediction of river corridor and watershed function. In *American geophysical union, fall general assembly.* doi: 10.1002/essoar.10500258.1

Schilling, O. S., Cook, P. G., & Brunner, P. (2019). Beyond classical observations in hydrogeology: the advantages of including exchange flux, temperature, tracer concentration, residence time, and soil moisture observations in groundwater model calibration. *Reviews of Geophysics*, *57*(1), 146–182. doi: 10.1029/2018RG000619

Schlichting, H. (1979). *Boundary layer theory* (7th ed.). New York: McGraw-Hill Publishing.

Smith, M. W. (2014). Roughness in the earth sciences. *Earth-Science Reviews*, *136*, 202–225. doi: 10.1016/j.earscirev.2014.05.016

Song, H. S., Cannon, W. R., Beliaev, A. S., & Konopka, A. (2014). Mathematical modeling of microbial community dynamics: A methodological review. *Processes*, *2*(4), 711–752. doi: 10.3390/pr2040711

Stegen, J. C., Fredrickson, J. K., Wilkins, M. J., Konopka, A. E., Nelson, W. C., Arntzen, E. V., ... Tfaily, M. (2016). Groundwater-surface water mixing shifts ecological assembly processes and stimulates organic carbon turnover. *Nature Communications*, *7*. doi: 10.1038/ncomms11237

Trinci, G., Harvey, G. L., Henshaw, A. J., Bertoldi, W., & Hölker, F. (2017). Life in turbulent flows: interactions between hydrodynamics and aquatic organisms in rivers. *Wiley Interdisciplinary Reviews: Water*, *4*(3), e1213. doi: 10.1002/wat2.1213

USACE. (1994). Hydraulics design of flood control channels. *US Army Corps of Engineers Engineer Manual*(, 1110-2-1601), 1–183.

Venditti, J. G., Dietrich, W. E., Nelson, P. A., Wydzga, M. A., Fadde, J., & Sklar, L. (2010). Mobilization of coarse surface layers in gravel-bedded rivers by finer gravel bed load. *Water Resources Research*, *46*(7), 1–10. doi: 10.1029/2009wr008329

Versteeg, H. K., & Malalasekera, W. (2007). *An introduction to computational*

fluid dynamics : the finite volume method (2nd ed.). England: Pearson Education Limited.

Wampler, P. J. (2012). Rivers and streams - water and sediment in motion. *Nature Education Knowledge*, *3*(10), 18.

Ward, A. S., & Packman, A. I. (2019). Advancing our predictive understanding of river corridor exchange. *Wiley Interdisciplinary Reviews: Water*, *6*(1), e1327. doi: 10.1002/wat2.1327

Wilcox, D. C. (2006). *Turbulence modeling for CFD* (3rd ed.). La Canada, Calif: DCW Industries.

Wilkes, M. A., Gittins, J. R., Mathers, K. L., Mason, R., Casas-Mulet, R., Vanzo, D., ... Jones, J. I. (2019). Physical and biological controls on fine sediment transport and storage in rivers. *Wiley Interdisciplinary Reviews: Water*, *6*(2), e1331. doi: 10.1002/wat2.1331

Yang, J. Q., & Nepf, H. M. (2018). A Turbulence-Based Bed-Load Transport Model for Bare and Vegetated Channels. *Geophysical Research Letters*, *45*(19), 10,428–10,436. doi: 10.1029/2018GL079319

Zalesak, S. T. (1979, jun). Fully multidimensional flux-corrected transport algorithms for fluids. *Journal of Computational Physics*, *31*(3), 335–362. doi: 10.1016/0021-9991(79)90051-2